Article:

Frankland, VL, James, AD, Carrillo-Sánchez, JD et al. (3 more authors) (2017) CO Oxidation and O2 Removal on Meteoric Material in Venus' Atmosphere. Icarus, 296. pp. 150-162. ISSN 0019-1035

https://doi.org/10.1016/j.icarus.2017.06.005

CO Oxidation and O_2 Removal on Meteoric Material in Venus' Atmosphere

Victoria L. Frankland [1], Alexander D. James [1], Juan Diego Carrillo-Sánchez [1],
David Nesvorný [2], P. Pokorný[3,4], and John M. C. Plane [1] *

[1] School of Chemistry, University of Leeds, Leeds, UK
[2] Department of Space Studies, SouthWest Research Institute, 1050 Walnut St., Suite 30, Boulder, USA
[3]The Catholic University of America, 620 Michigan Ave, 20064, Washington D.C., USA
[4] Space Weather Laboratory, Mail Code 674, GSFC/NASA, Greenbelt, Maryland, USA
* Corresponding author (j.m.c.plane@leeds.ac.uk)

Abstract

The heterogeneous oxidation of CO by O_2 on olivine, Fe sulfate and Fe oxide particles was studied using a flow tube apparatus between 300 and 680 K. These particles were chosen as possible analogues of unablated cosmic dust and meteoric smoke in Venus' atmosphere. On olivine and Fe oxides, the rate of CO oxidation to CO_2 only becomes significant above 450 K. For iron sulfates, CO_2 production was not observed until these dust analogues had decomposed into iron oxides at ~ 540 K. The CO oxidation rate increases significantly with a higher Fe content in the dust, implying that oxidation occurs through Fe active sites (no reaction was observed on Mg_2SiO_4). The oxidation kinetics can be explained by CO reacting with chemi-sorbed O_2 through an Eley-Rideal mechanism, which is supported by electronic structure calculations. Uptake coefficients were measured from 450 to 680 K, yielding:

$\log_{10}(\gamma(\mathrm{CO\ on\ MgFeSiO_4})) = (2.9 \pm 0.1) \times 10^{-3}\ T(\mathrm{K}) - (8.2 \pm 0.1)$;

$\log_{10}(\gamma(\mathrm{CO\ on\ Fe_2SiO_4}) = (2.3 \pm 0.3) \times 10^{-3}\ T(\mathrm{K}) - (7.7 \pm 0.2)$;

$\log_{10}(\gamma(\mathrm{CO\ on\ FeOOH/Fe_2O_3}) = (5.6 \pm 0.8) \times 10^{-3}\ T(\mathrm{K}) - (9.3 \pm 0.4)$.

A 1-D atmospheric model of Venus was then constructed to explore the role of heterogeneous oxidation. The cosmic dust input to Venus, mostly originating from Jupiter Family Comets, is around 32 tonnes per Earth day. A chemical ablation model was used to show that ~34% of this incoming mass ablates, forming meteoric smoke particles which, together with unablated dust particles, provide a significant surface for the heterogeneous oxidation of CO to CO_2 in Venus' troposphere. This process should cause almost complete removal of O_2 below 40 km, but have a relatively small impact on the CO mixing ratio (since CO is in large excess over O_2). Theoretical quantum calculations indicate that the gas-phase oxidation of CO by SO_2 in the lower troposphere is not competitive with the heterogeneous oxidation of CO. Finally, the substantial number density of meteoric smoke particles predicted to occur above the cloud tops may facilitate the low temperature heterogeneous chemistry of other species.

Keywords: Venus Atmosphere; Cosmic dust; Experimental techniques

1. Introduction

The most abundant atmospheric species in Venus' atmosphere are CO_2 (96.5%) and N_2 (3.5 %) (Bezard and de Bergh, 2007). Despite CO_2 undergoing photolysis, Venus has maintained its CO_2-rich atmosphere over geological timescales. Photolysis occurs *via* solar ultraviolet light at wavelengths below 200 nm, forming CO and atomic O. This process occurs mainly above the top of the sulfuric acid cloud and haze layers (> 65 km), since these aerosols reduce the UV solar flux in the lower atmosphere (Krasnopolsky, 2012). O atoms rapidly recombine to form O_2. The current abundance of CO (45 ppm at the cloud tops) would be produced in only ~200 yrs (Taylor, 2010).

Curiously, the O_2 mixing ratio is much less than half that of CO, which is the value that would be expected based on this simple photochemistry. Trauger and Lunine (1983) used terrestrial spectroscopic observations to determine an upper limit to the mixing ratio of O_2 immediately above the clouds of only 0.3 ppm, in good agreement with an earlier study (Traub and Carleton, 1974). In contrast, gas chromatographic measurements by the Pioneer Venus sounder probe reported O_2 mixing ratios of 44 and 16 ppm at heights of 52 and 44 km, respectively (Oyama et al., 1980). This result is difficult to reconcile with the above-cloud measurements, since this is where the source of the O_2 should be (Trauger and Lunine, 1983; von Zahn et al., 1983; Krasnopolsky, 2012). In any case, there must be efficient routes to re-oxidise CO and remove O_2; indeed, O_2 above the clouds is currently over-predicted in atmospheric models by an order of magnitude relative to the upper limit (Krasnopolsky, 2012).

CO oxidation cannot occur through the spin-forbidden recombination of CO with O in the gas phase, and the gas-phase reaction between CO and O_2 has an activation energy of around 200 kJ mol^{-1} and is thus extremely slow except possibly close to the surface of Venus (Tsang and Hampson, 1986). Instead, a chlorine-catalyzed cycle has been proposed which involves formation of the ClCO intermediate followed by reaction with O_2 (Mills and Allen, 2007; Krasnopolsky, 2012):

$$\mathrm{Cl + CO\ (+\ M) \rightarrow ClCO} \qquad \text{(R1)}$$

$ClCO + O_2 \rightarrow CO_2 + ClO$ (R2)

where R2 proceeds via the $ClCO_3$ intermediate (Pernice et al., 2004). This appears to be the primary CO oxidation pathway above 65 km. Because the OH radical concentration (~10^3 cm^{-3} at 70 km) is low relative to Cl (~10^{10} cm^{-3} at 70 km) in Venus' atmosphere, the reaction

$OH + CO \rightarrow CO_2 + H$ (R3)

must play a secondary role (Krasnopolsky, 2012). Below the clouds (< 38 km) where the temperature increases above 400 K, SO_2 has been proposed as a significant oxidant (reaction R4) (Fegley et al., 1997):

$CO + SO_2 \rightarrow CO_2 + SO$ (R4)

Previous attempts to understand this atmospheric CO chemistry have focused on comparing these gas-phase mechanisms in atmospheric models. However, CO oxidation can also occur catalytically on a surface at high temperatures in the presence of O_2, including the proposed oxidation of CO on hematite at the Venusian surface (Grenfell et al., 2010; Grenfell et al., 2013). The oxidation can take place either through the Langmuir-Hinshelwood mechanism, which involves both species adsorbing on the surface and then diffusing together before reacting; or via the Eley-Rideal mechanism, where reaction occurs between one of the reactants adsorbed on the surface and the second directly from the gas phase (Kolasinski, 2002). There is a large body of research from the automotive industry on CO oxidation by platinum group metal-containing materials (Kašpar et al., 2003), though much less on materials with base metals such as Fe which tend to be poisoned by SO_2 in vehicle exhausts (Wang, 2006).

In this paper we consider the heterogeneous oxidation pathway of CO by O_2 on meteoric material in Venus' atmosphere. This material will be both un-ablated meteoroids and the meteoric smoke particles (MSPs) which form from the oxidation and subsequent condensation of ablated meteoric metals. These nm-sized particles are probably composed of olivines ($Mg_{2-2n}Fe_{2n}SiO_4$ where $O \leq n \leq 1$) or Fe-Mg oxides (Saunders and Plane, 2006).

To the best of our knowledge, there are no studies of CO oxidation on olivines in the literature. However, CO_2 formation on hematite (α-Fe_2O_3) has been studied previously: in addition to a low temperature (196 K) study of CO uptake on Fe_2O_3 and Fe_3O_4 (Leu et al., 1992), Grenfell et al. (2013) and Grenfell et al. (2010) used the experimental work of Wagloehner et al. (2008) to show that the CO oxidation data was better modelled assuming the Eley-Rideal mechanism with gaseous CO molecules reacting directly with adsorbed O_2. The diffusion of adsorbed O_2 (or O if the molecule dissociated on the surface) on α-Fe_2O_3 was not considered to be significant i.e. the O_2 was confined to the active adsorption sites (Randall et al., 1997).

Calculations performed by Wu et al. (2015) for CO oxidation on a graphyne-supported single Fe atom found that O_2 bonds more strongly than CO to the Fe atom, resulting in the incoming CO molecules reacting with adsorbed O_2 *via* the Eley-Rideal mechanism. In contrast, Khedr et al. (2006) found that CO_2 formation on Fe_2O_3 nanoparticles occurred through the Langmuir-Hinshelwood mechanism, with CO reacting with dissociated O_2 molecules bound on Fe active sites. A theoretical study by Bulgakov and Sadykov (1996) assigned CO oxidation to the existence of defect centres or centres located on stepped planes on α-Fe_2O_3 surfaces.

In the present study, meteoroids and MSPs were represented by synthetic olivine ($MgFeSiO_4$), forsterite (Mg_2SiO_4) and fayalite (Fe_2SiO_4) analogues. In Venus' atmosphere, these particles will sediment through the H_2SO_4 cloud layers between ~38 and 65 km (Knollenberg and Hunten, 1980), which may chemically alter their composition through dissolution in H_2SO_4/H_2O droplets and precipitation of sulfate salts on evaporation of the liquid droplets, in a similar way to that proposed in Earth's atmosphere (Saunders et al., 2012). Thus, CO oxidation within the H_2SO_4 clouds was explored on ferric ($Fe_2(SO_4)_3$) and ferrous sulfate ($FeSO_4$) analogues. At the higher temperatures below the clouds, Fe sulfate particles will decompose into Fe oxides (as demonstrated in the present study). Fe oxides were represented with a synthetic goethite (FeOOH) analogue which dehydrates into hematite (α-Fe_2O_3).

The experiments were performed using a flow tube technique combined with mass spectrometry (Section 2). The mechanism with of CO oxidation was investigated (Section 3) and the experimental uptake coefficients are then included in a 1D model of meteoric dust transport in Venus' atmosphere in order to assess the potential impacts on CO oxidation and O_2 removal (Section 4).

2. Experimental Method

A schematic diagram of the flow tube apparatus used to measure uptake coefficients on meteoric dust analogues is shown in Figure 1. The quartz flow tube is 50 cm in length with an internal diameter of 1 cm. The middle section of the flow tube (38 cm in length) was wrapped in heating tape and Rockwool pipe insulation, enabling the flow tube temperature to be varied between room temperature and 680 K. A K-type thermocouple located inside the heated part of the flow tube was used to monitor the temperature of the dust analogue surface.

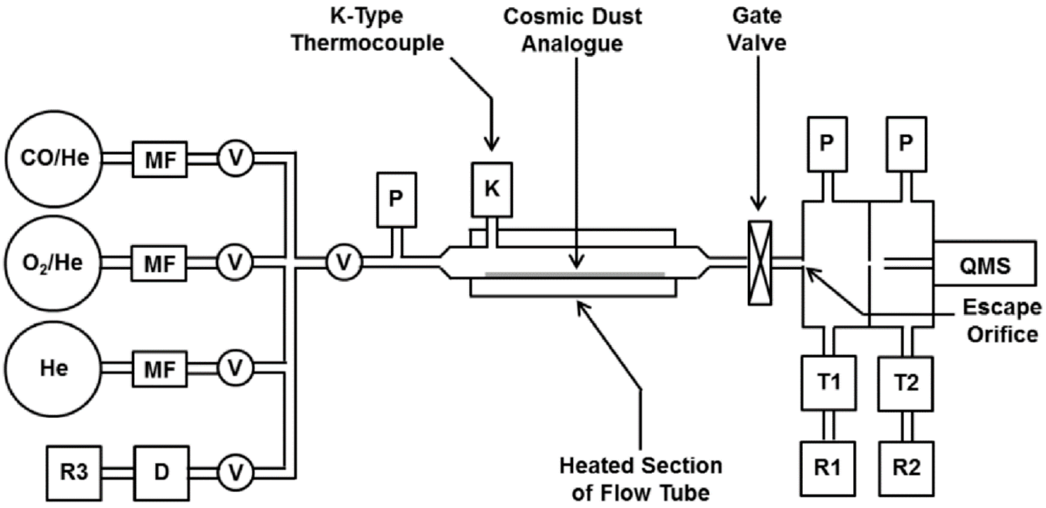

Figure 1. Schematic diagram of the flow tube apparatus where MF denotes a mass flow controller, V a 2- way valve, P a pressure gauge, K a K-type thermocouple, QMS the quadrupole mass spectrometer and D, T and R are diffusion, turbo and rotary pumps, respectively.

Attached to the flow tube is a stainless steel and glass gas-handling line fitted with mass flow (MF) controllers (MKS Instruments, 20, 100 and 200 sccm). Pressure was measured by a Baratron gauge (MKS, 0-1000 Torr) just upstream of the flow tube. Downstream, the flow tube is coupled to a double differentially pumped vacuum chamber equipped with a quadrupole mass spectrometer (QMS) (VG Quadrupoles, SXP Elite). The entrances to the first and second differentially pumped chambers are separated by flanges with orifices of 0.3 and 1.2 mm diameter, respectively.

Of the meteoric material analogues used in this study, four were synthetic: $MgFeSiO_4$; Mg_2SiO_4; Fe_2SiO_4; and FeOOH. Each of the metal silicate analogues were prepared using sol-gel techniques by mixing solutions in stoichiometric amounts under stirring at room temperature of magnesium chloride ($MgCl_2$) (Aldrich), ferrous (II) ammonium sulphate ($Fe(NH_4)_2(SO_4)_2$) (Sigma-Aldrich) and sodium orthosilicate (Na_4SiO_4) (Alfa Aesar). These solutions were stirred at room temperature for 7 days to allow the reaction to go to completion. Metal-salt by-products were removed from all of the synthetic analogues by repeated dialysis using a soxhlet apparatus with the particles held in water permeable tubing (Snakeskin, 7000 MWCO) for 12-16 hours. The products were then stored in a desiccator. Goethite (FeOOH) was produced by stirring a solution of 0.1 mol l^{-1} each of $Fe(SO_4)_2(NH_4)_2$ and NaOH for 3 days with a flow of compressed air bubbling through the reacting solution. The purified goethite product of this reaction was dehydrated by annealing at 573 K for 24 hours to produce hematite (Fe_2O_3). These syntheses provide large quantities (10s g) of appropriate, well-characterised analogues for bulk surface science work. Further details of the preparation and characterisation of these amorphous materials with large specific surface areas are provided in James et al. (2016). In order to explore the effect of the chemical alteration of MSPs in the sulfuric acid clouds and haze layers in Venus' atmosphere, the dust analogues ferric sulfate ($Fe_2(SO_4)_3$) (BDH Chemicals Ltd.) and ferrous sulfate heptahydrate ($FeSO_4$) (Arcos Organics) were used.

The physical and chemical characterisation of all the analogues used in this study (both before and after each experiment) were explored using several techniques (see Table 1). Morphology and elemental composition were obtained using transmission electron microscopy (TEM) combined with energy-dispersive X-ray spectroscopy (EDX) (FEI Tecnai F20 200 kV FEGTEM fitted with a Gantan Orius SC600 CCD camera and an Oxford Instruments X-Max 80 mm^2 SDD EDX). These results were combined with the crystal structure analysis, obtained by X-ray diffraction (XRD) (Brucker, D8 Advance with a Cu Kα X-ray source), to constrain the nature of each analogue. The XRD analysis also showed that the metal-silicate analogues were amorphous. The dust specific surface area, $a_{(BET)}$, was obtained *via* the Brunauer-Emmet-Teller (BET) isotherm (Micrometrics, ASAP 2020). The bulk density of each analogue (i.e. the density of the dust analogue particles in air) was measured by placing a known mass of sample in a measuring cylinder, so that the volume accessible to the gas in the flow tube could be calculated. The flow tube geometry was also used to estimate the surface area of the 0.5 g sample of each dust analogue exposed to the gas flow, where the dust was spread uniformly along the bottom of the flow tube. This yielded a minimum dust surface area, $a_{(GEO)}$, assuming no porosity and a flat surface. The validity of these $a_{(GEO)}$ values in relation to a realistic, textured surface is discussed in Section 3.3.

Table 1. BET surface area, $a_{(BET)}$, bulk mass densities and the geometric surface area $a_{(GEO)}$ (0.5 g sample in the flow tube) for each cosmic dust analogue.

Cosmic Dust Analogue	$a_{(BET)}$ / m^2 g^{-1}	Bulk Density / g cm^{-3}	$a_{(GEO)}$/ cm^2
Mg_2SiO_4	102.2±5.1	0.82±0.03	17.0
$MgFeSiO_4$ (300 K)	358.1±16.1	0.88±0.03	16.6
(heated to 656 K)	156.9±4.87		
Fe_2SiO_4 (300 K)	244.3±2.3	0.72±0.03	17.9
(heated to 683 K)	208.2±2.1		
$FeOOH/Fe_2O_3$ (unheated)	41.4±0.4	0.78±0.03	16.7
(heated to 495 K with CO and O_2)	93.9±2.8		
(heated to 550 K with CO and O_2)	104.9±3.0		
(heated to 636 K with CO)	34.4±0.2		
$Fe_2(SO_4)_3$ (unheated)	8.4±0.1	0.80±0.03	17.2
(heated to 698 K)	16.9±0.2		
$FeSO_4$ (unheated)	45.6±0.1	1.06±0.04	15.7
(heated to 689 K)	5.9±0.1		

CO (>99.0 %, SAFC) and O_2 (>99.999 %, BOC) were each diluted in He (CP grade, BOC) to a mixing ratio of 0.0134 using standard manometric techniques. In a typical experiment, 8.4 and 4.2 sccm of the CO/He and O_2/He gas mixtures, respectively, were introduced into the flow tube simultaneously to provide a 2:1 ratio consistent with the stoichiometry of the overall $2CO + O_2 \rightarrow 2CO_2$ reaction. In some experiments this ratio was varied in order to investigate the kinetic order dependence and a balancing He flow was then used to maintain constant pressure.

In a typical experiment, 0.5 g of a particular dust analogue was evenly distributed into the heated section of the flow tube before degassing by pumping overnight. The flow tube was heated to the selected temperature and allowed to stabilise for at least 30 minutes. The CO, O_2 and CO_2 mass traces were then monitored for approximately 2 minutes to obtain background counts, before introducing the CO and O_2 flows into the flow tube. Here, the pressure inside the flow tube rose to ~10 Torr; at this relatively low pressure, diffusion of reactants through the gas phase does not kinetically limit the uptake process. Once the mass traces had stabilised, the data was collected for a minimum of 5 minutes before terminating the gas flow. After the mass traces decreased to a minimum they were once again monitored for background correction. The uptake of CO and O_2 onto the flow tube walls was determined by repeating all the experiments with the same procedure, but without a dust sample in the flow tube. Once background corrected, the empty flowtube data was subtracted from the background corrected dust data to determine the changes to the CO, O_2 and CO_2 caused by CO oxidation on the dust analogue. After each experiment, the sample was recovered for compositional, structure and BET analysis.

3. Results and Discussion

The proposed mechanism for the heterogeneous oxidation of CO on these dust samples is shown by reactions R5 to R7. The evidence supporting this mechanism is presented in the following sub-sections. The subscripts *g* and *ads* denote molecules in the gas phase and adsorbed to the dust surface, respectively. Based on a review of the literature (see Section 1), adsorption of O_2 at these elevated temperatures most likely involves chemisorption to an Fe active site. Once bound, the O_2 molecules remain confined to these surface sites (e.g. Randall et al. (1997)), until reaction with gas-phase CO molecules through the Eley-Rideal mechanism (reactions 6 and 7). The CO molecules remove each O atom in succession, with reaction 6 being the overall rate-determining step. Electronic structure calculations are presented in Section 3.6 to support this mechanism and interpret the experimental observations.

$$O_{2(g)} \rightarrow O_{2(ads)} \qquad \text{(R5)}$$

$$CO_{(g)} + O_{2(ads)} \rightarrow CO_{2(g)} + O_{(ads)} \qquad \text{(R6)}$$

$$CO_{(g)} + O_{(ads)} \rightarrow CO_{2(g)} \qquad \text{(R7)}$$

3.1. Fe Active Site Dependence

Figure 2 illustrates the concentration of CO_2 downstream of the flow tube as a function of temperature, for 0.5 g of each of the analogue dust samples. On $MgFeSiO_4$ and Fe_2SiO_4, the CO_2 mass trace became detectable above the noise at ~450 K, and appears to plateau around 680 K. About 50% less CO_2 is produced on $MgFeSiO_4$ compared with Fe_2SiO_4, and none was detected on Mg_2SiO_4. This implies that the surface reaction is governed by the availability of Fe active surface sites. The amount of CO_2 formed on the $FeSO_4$ and $Fe_2(SO_4)_3$ samples is approximately 1 and 2 orders of magnitude smaller, respectively, than that formed on Fe_2SiO_4. These differences could be due to the smaller BET surface areas of the sulphate particles (Table 1), and a lower oxidation efficiency of the Fe^{3+} ions in $Fe_2(SO_4)_3$.

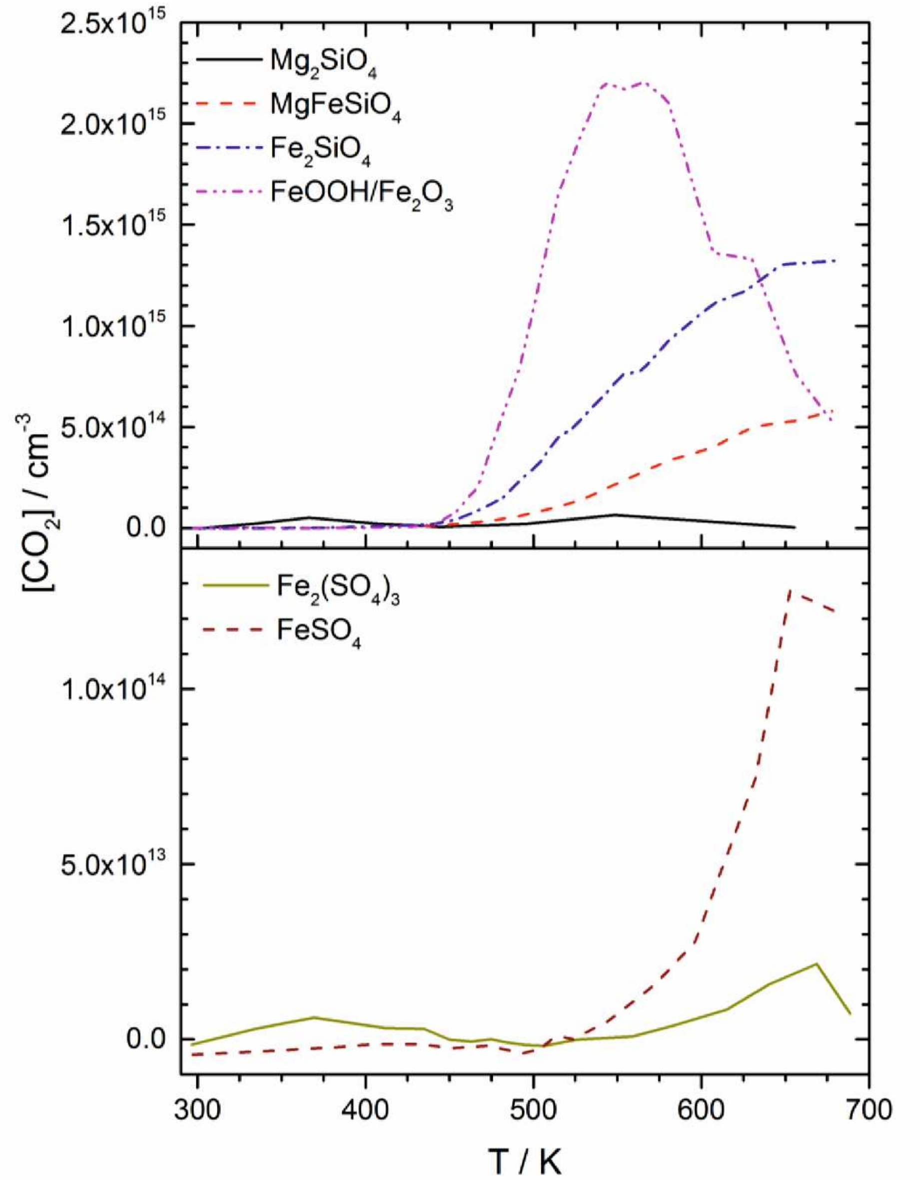

Figure 2. The CO_2 concentration produced from each dust analogue, as a function of temperature in the flow tube.

CO_2 production on $FeSO_4$ and $Fe_2(SO_4)_3$ is not apparent until around 540 K. From 450 to 540 K, a small drop in the CO mass trace was detected in the experiments with $FeSO_4$ in the flow tube, indicating adsorption of CO although no CO_2 production was observed. The onset of CO_2 production coincides with the decomposition of the sulfates to oxides. This was shown by a colour change in the dust samples (turquoise green to pale yellow for $FeSO_4$; ivory to pale caramel for $Fe_2(SO_4)_3$). XRD analysis confirmed that $FeSO_4$ had partly decomposed to Fe oxides (including α-Fe_2O_3), and SO_2 production was observed from 540 K when CO_2 became detectable. This process is hypothesised to occur through the following reactions:

$$FeSO_4 \rightarrow SO_2 + FeO_2 \quad \text{(R8)}$$

$$2FeO_2 + CO \rightarrow \alpha\text{-}Fe_2O_3 + CO_2 \quad \text{(R9)}$$

CO oxidation on FeOOH is complex as FeOOH dehydrates to hematite (α-Fe_2O_3) at elevated temperatures (Cornell and Schwertmann, 2003), so hereafter this dust analogue will be referred to as FeOOH/Fe_2O_3. Overall, a faster rate of CO oxidation was detected on FeOOH/Fe_2O_3 compared to Fe_2SiO_4 (Figure 2), despite FeOOH having a BET surface area, $a_{(BET)}$, ~ 6 times smaller than Fe_2SiO_4 (Table 1). The temperature at which the CO_2 mass trace became detectable above the noise was similar to that of Fe_2SiO_4 and $MgFeSiO_4$. The CO oxidation rate peaks at ~ 550 K; the decrease at higher temperatures is probably due to sintering of the dust causing the observed reduction of the BET surface area.

3.2. O_2 Uptake to Fe Active Sites

A key observation in these experiments was a delay in the O_2 mass trace despite the O_2/He and CO/He gas mixtures being introduced to the dust analogue at the same time (Figure 3). This delay, which was typically around 5 s on Fe_2SiO_4, implies that O_2 molecules are preferentially and rapidly adsorbed on the Fe active sites, and hence O_2 does not emerge at the downstream end of the flow tube until all these sites have been occupied (this is modelled in Section 3.3). The delay in O_2 has also been observed by Wagloehner et al. (2008) and Wu et al. (2015) for CO oxidation by O_2 on α-Fe_2O_3 and pure Fe, respectively. Note that the rapid uptake of O_2 to the empty Fe active sites indicates that O_2 adsorption is not the rate-determining step in the CO oxidation mechanism under these experimental conditions. Since the distance between adjacent surface Fe atoms on these dust minerals (4.82 Å for Fe_2SiO_4 (Hazen, 1977); 6.50 Å for $FeSO_4$ (Anderson et al., 2007); 3.01 Å for FeOOH and 5.03 Å for α-Fe_2O_3 (Cudennec and Lecerf, 2005)) are much larger than the O-O bond distance (1.21 Å), it seems unlikely that an adsorbed O_2 would stretch across adjacent Fe atoms and dissociate.

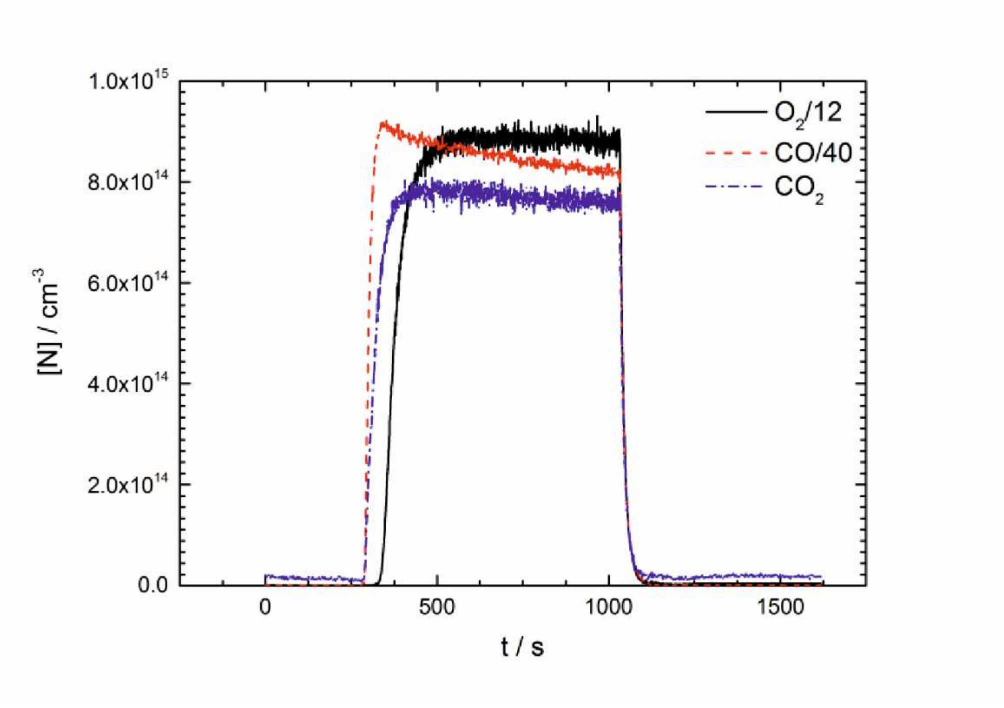

Figure 3. O_2, CO and CO_2 in a typical experiment on Fe_2SiO_4 indicating the delay in the O_2 mass trace with respect to CO and CO_2.

3.3. Surface Area Available for CO Oxidation

The rate of uptake of a gas to a solid surface is characterised by the uptake coefficient, γ, defined as the probability that a collision will result in the loss of a molecule from the gas phase. In this experimental set-up, γ can be calculated from the expression:

$$\gamma = \frac{4F}{\bar{c}a_s} ln\left(\frac{[N_0]}{[N_\tau]}\right) \tag{1}$$

where *F* is the total flow rate through the flow tube (in cm^3 s^{-1}); $\bar{c}$ is the molecular mean speed (cm s^{-1}); a_s the surface area available for uptake (cm^2); and [N_0] and [N_τ] are the concentrations of species *N* upon entering and exiting the flow tube, respectively (τ is the residence time of the species *N* in the flow tube). [N_0] and [N_τ] were taken as the CO mass signals in the experiments without and with dust, respectively. *F* was obtained by correcting the calibrated mass flow controller settings for the experimental temperature and pressure.

One potential complication with this technique is knowing the fraction of the dust surface area which is available for the uptake of O_2 and CO. At one extreme, if the gas is readily taken up then it will only be the particles in the uppermost layers of the sample which will be directly involved. At the other extreme, an unreactive gas will penetrate throughout the sample and be exposed to the full surface area of the dust analogue particles.

Possible values of a_s range from the geometric surface area, $a_{(GEO)}$ (the surface area of the dust sample inside the heated region of the flow tube if a smooth ideal surface is assumed – see Table 1), to the surface area given by the Brunauer-Emmet-Teller isotherm, $a_{(BET)}$. Measured values of $a_{(BET)}$ with respect to temperature (to account for thermal processing of the dust analogues) are listed in Table 1. It should be noted that annealing $MgFeSiO_4$ in an oven at 1027 K for 48 hours did not reduce the surface area by more than the factor of 2 shown in Table 1 for 30 mins at 656 K.

$a_{(GEO)}$ and $a_{(BET)}$ were varied by varying the sample mass of $MgFeSiO_4$ from 0.1 to 3.5 g at 490 K (at which temperature the BET surface area was not significantly different than that measured before exposure to high temperatures). The results are plotted in Figure 4 with the error in γ calculated from the error in the CO_2 concentration which was taken as one standard deviation of the mean between repeats. The upper plot shows there is no variation in $\gamma(a_{(GEO)})$ with respect to $a_{(GEO)}$. Taking the assumption that $a_s=a_{(BET)}$, the number of active sites for CO oxidation should increase linearly with the available mass. The lower panel shows a physically unreasonable variation of γ ($a_{(BET)}$) with the total available surface area (hence no fit was applied to Figure 4b). This suggests that the surface area available for CO oxidation is significantly less than $a_{(BET)}$, and is much closer to $a_{(GEO)}$. A similar result was obtained with the FeOOH/Fe_2O_3 dust.

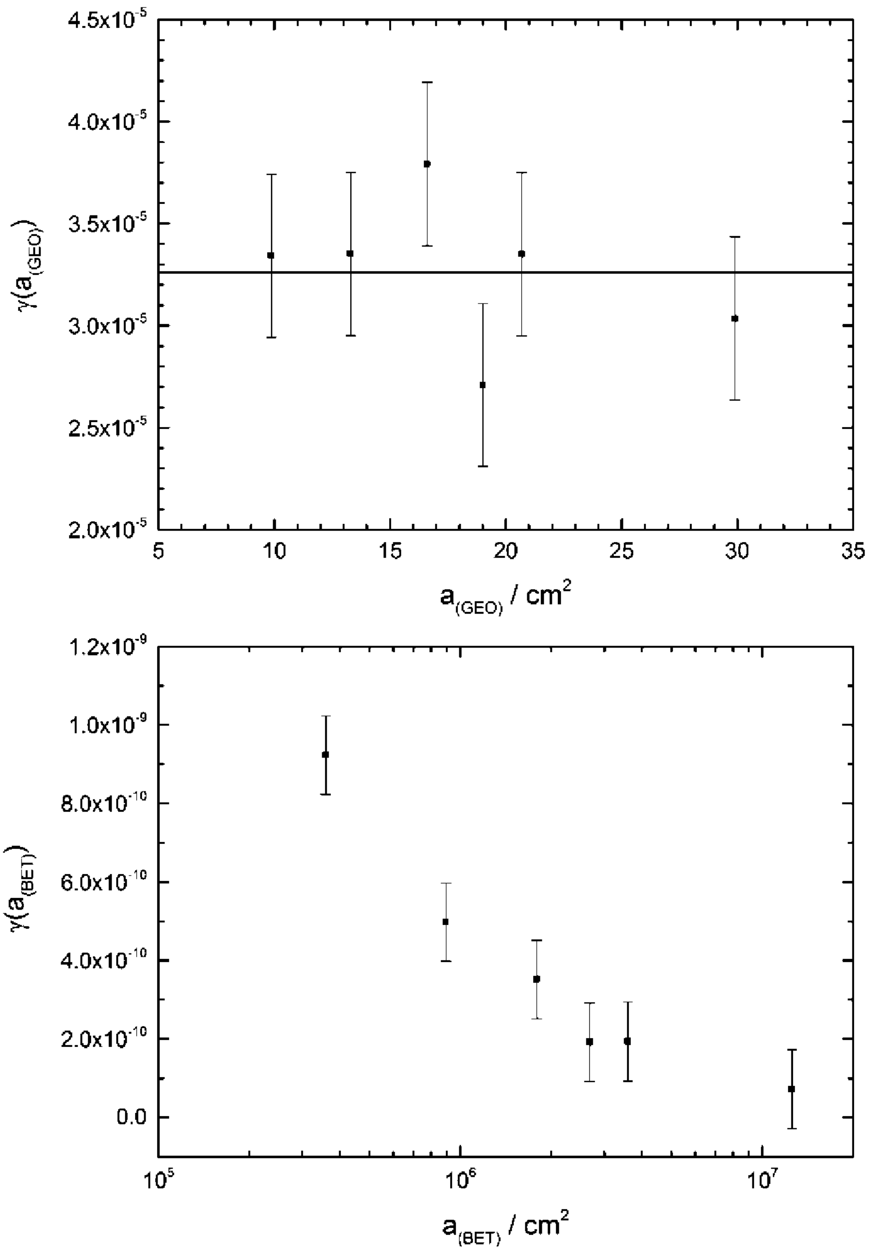

Figure 4. The uptake coefficient, γ, of CO on $MgFeSiO_4$ at 490 K as a function of dust surface area. The top panel shows γ calculated using the geometric surface area, *a(GEO)*, which yields an upper limit; the bottom panel shows γ calculated using the BET surface area, *a(BET)*, which yields a lower limit for γ.

The available surface area can also be estimated from the observed delay in the O_2 signal when the CO and O_2 flows are first switched on simultaneously (see Section 3.2 and Figure 3). The observed O_2 signal delay indicates that the O_2 molecules were taken up on the surface but, after some time, the surface reached an equilibrium between uptake of O_2 and production of CO_2, the latter reactivating available surface sites. The amount of O_2 which was required to saturate the surface was calculated from the O_2 mixing ratio in the gas flow and the flow rate through the reactor. This amount of saturated O_2 was converted into a surface density based on the value of $a_{(GEO)}$ for the analogue being used. Assuming that only a single O_2 molecule occupied each Fe active site on the analogue surface, the adjustment required to get the available reactive surface area, a_r, from $a_{(GEO)}$ was obtained by taking the ratio of the surface densities of O_2 to Fe for each analogue.

In the case of Fe_2SiO_4, the surface density of adsorbed O_2 is 54 times larger than that of Fe active sites (Hazen, 1977). This implies, as expected, that the rough surface area provided by an assemblage of particles provides a considerably larger reactive surface area a_r, which we define as $a_r = 54a_{(GEO)}$. For a 0.5 g sample of Fe_2SiO_4, $a_{(GEO)}$ is 17.9 cm^2 and so a_r is 967 cm^2. Note that this is much smaller than $a_{(BET)} = 1.2 \times 10^6$ cm^2 (Table 1). The surface density of Fe active sites in the synthesized $MgFeSiO_4$ analogue is not known, and so it was assumed here that the closest distance between two Fe active sites on the surface is the same as that for Fe_2SiO_4 i.e. a_r for $MgFeSiO_4$ was taken as $54a_{(GEO)}$, which is possibly a lower limit.

The O_2 time delay for $FeSO_4$ was below that of the QMS time resolution (0.6 s), giving a lower limit for $a_r(FeSO_4)$ of $17a_{(GEO)}$. The O_2 time delay on $FeOOH/Fe_2O_3$ varied between 2 and 121 s depending on T, so that a_r varied between $16a_{(GEO)}$ to $928a_{(GEO)}$. A possible explanation for this variation in a_r is that the crystal structure of this dust analogue changes as FeOOH dehydrates to α-Fe_2O_3 with respect to time and temperature (Cornell and Schwertmann, 2003). Note that these values of a_r for FeOOH/Fe_2O_3 dust are a relatively small increase in a_s compared to the upper limit given by $a_{(BET)}$, suggesting that that the increase from a_s to a_r is likely due to surface roughness and the CO oxidation occurring in the few uppermost layers of the particles.

Using a_r, we can now estimate a lower limit to the uptake coefficient for O_2 on olivine, $\gamma(O_2)$. A kinetic uptake model of the flow tube was constructed with a_r = 967 cm^2 (see above). The radius of each adsorption site was set equal to 3 Å, roughly half the distance between adjacent surface Fe atoms in Fe_2SiO_4 (Hazen, 1977). Figure 5 shows the modelled O_2 concentration in the downstream flow for a range of $\gamma(O_2)$, plotted as a function of time after CO first appears (see the figure caption for experimental details). This figure demonstrates that $\gamma(O_2)$ must be larger than 2×10^{-5} in order to explain the observed time delay of 5 s.

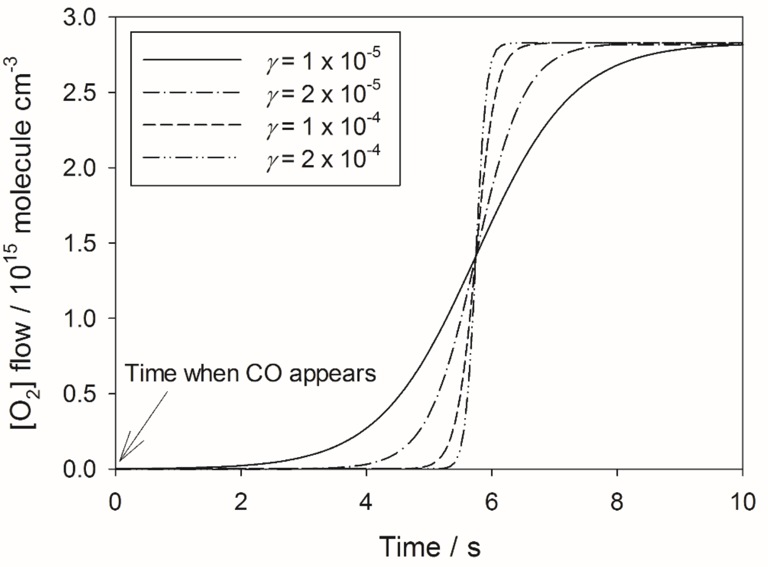

Figure 5. Modelled concentration of O_2 exiting the flow tube as a function of time after CO first appears, for a range of $\gamma(O_2)$ on Fe_2SiO_4. Conditions: T = at 500 K; pressure = 10 torr; total flow = 12.2 cm^3 s^{-1}; O_2 mixing ratio = 0.0165.

Another consequence of the surface being saturated with chemisorbed O_2 molecules is that the incoming CO molecules would be unable to adsorb and diffuse across the dust analogue surface. Thus, the CO oxidation was assumed to follow the Eley-Rideal (reaction without prior accommodation of one of the reactants on the surface) rather than the Langmuir-Hinshellwood surface mechanism. This is in agreement with the recent work of Grenfell et al. (2013) and Wu et al. (2015).

3.4. CO Oxidation as the Rate Determining Step

As discussed earlier in Section 3, the reaction of CO with adsorbed O_2 is assumed to be the rate-determining step in the overall oxidation of CO. Further evidence for this was obtained by examining the kinetic order dependence of CO_2 formation on [CO] and [O_2]. This was explored on $MgFeSiO_4$ at 490 and 550 K (Figure 6), and on FeOOH/Fe_2O_3 at 495 and 550 K (Figure 7) with the error taken as one standard deviation of the mean CO_2 concentration between repeats. Both dust samples (at all temperatures) showed a first-order dependence on CO (note the break in the ordinate axis of the CO plot in Figure 6). For O_2, the slopes are close to zero within error, indicating that the O_2 dependence is zeroth order on $MgFeSiO_4$ at both temperatures, and on FeOOH/Fe_2O_3 at 495 K. The same kinetic order behaviour for CO and O_2 has been observed previously on superfine maghemite (γ-Fe_2O_3) nanoparticles at 517 K (Li et al., 2003). The change in kinetic behaviour with respect to O_2 on FeOOH/Fe_2O_3 at 550 K could be due to the dust analogue having full transformed to α-Fe_2O_3.

375

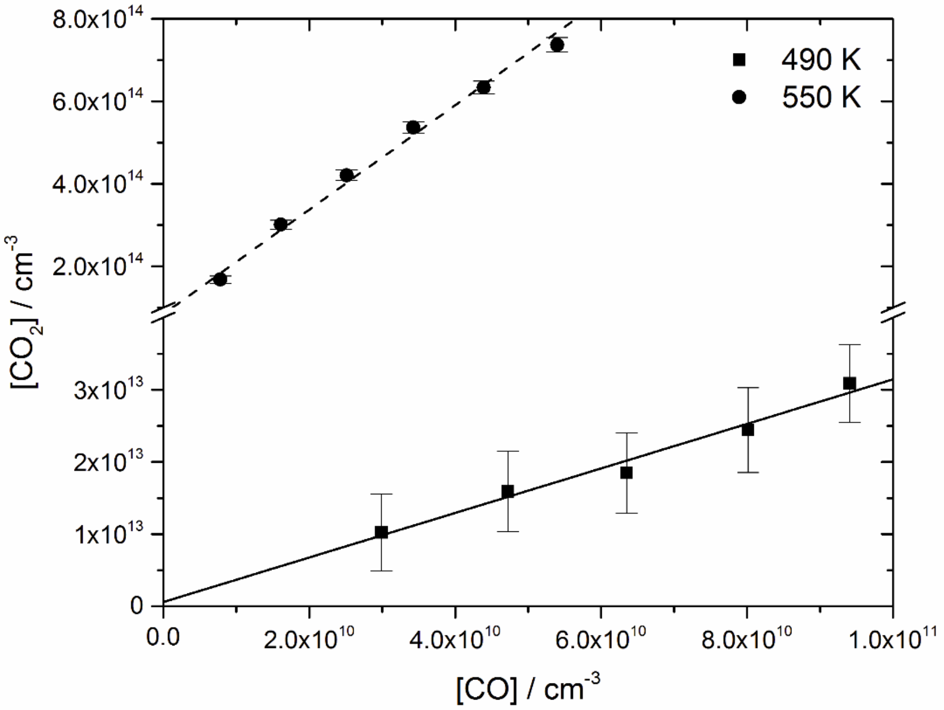
8.0x10^14
6.0x10^14
4.0x10^14
2.0x10^14
3x10^13
2x10^13
1x10^13
0
[CO2] / cm-3
0.0
2.0x10^10
4.0x10^10
6.0x10^10
8.0x10^10
1.0x10^11
[CO] / cm-3
■ 490 K
● 550 K

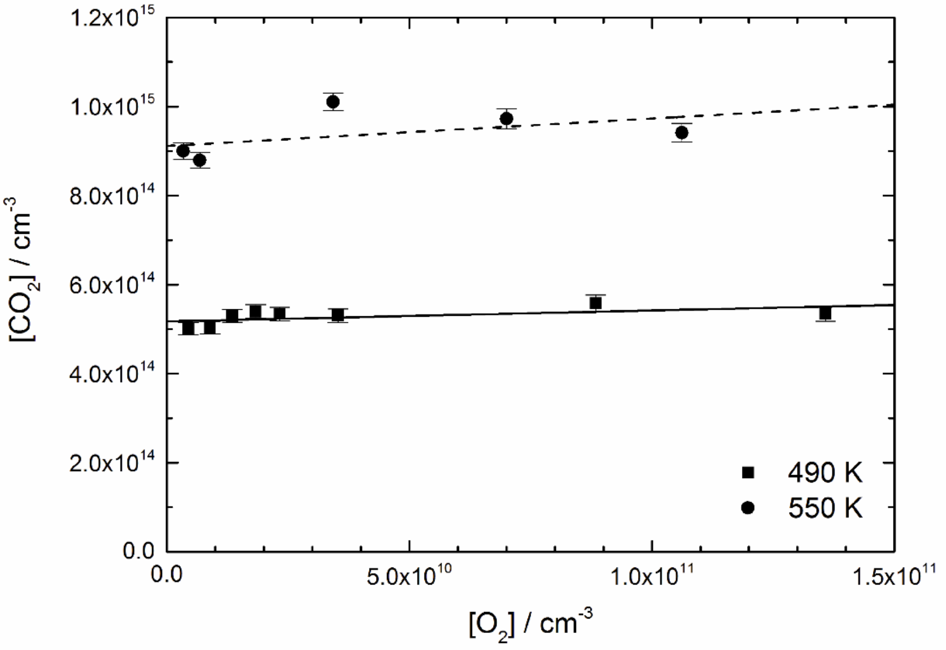
1.2x10^15
1.0x10^15
8.0x10^14
6.0x10^14
4.0x10^14
2.0x10^14
0.0
[CO2] / cm-3
0.0
5.0x10^10
1.0x10^11
1.5x10^11
[O2] / cm-3
■ 490 K
● 550 K

376

Figure 6. Dependence of CO_2 formation on CO (top – note the break in the ordinate axis) and O_2 (bottom) for $MgFeSiO_4$ at 490 K and 550 K. The lines are linear regression fits to the data at 490 K (solid) and 550 K (dashed).

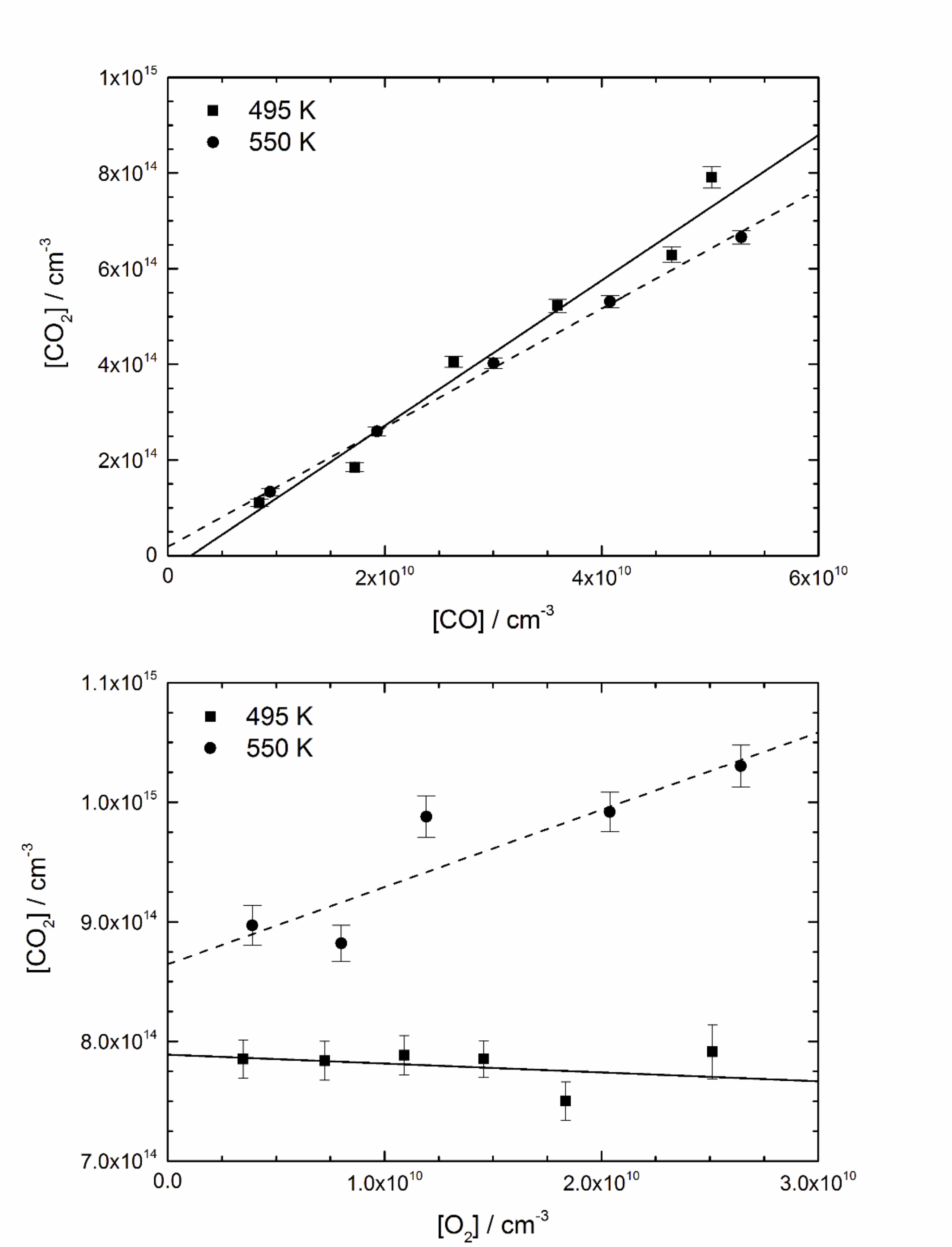

Figure 7. Dependence of CO_2 formation on CO (top) and O_2 (bottom) for FeOOH/Fe_2O3 at 495 K and 550 K. The lines are linear regression fits to the data at 490 K (solid) and 550 K (dashed).

3.5. Temperature dependence of uptake

For each dust where significant uptake was observed, the uptake coefficient was calculated using equation 1 with a_s taken as a_r for that dust analogue (Section 3.3). Figure 8 shows that γ(CO) increases exponentially with temperature. Because CO_2 production was not observed until $FeSO_4$ had decomposed into Fe oxides (section 3.1), $FeSO_4$ is excluded from Figure 8. $MgFeSiO_4$ has a similar slope but lower γ(CO) compared to Fe_2SiO_4. Regression fits though each data set between 450 and 700 K yield:

$\log_{10}(\gamma(\text{CO on } MgFeSiO_4)) = (2.9 \pm 0.1) \times 10^{-3}\ T(\text{K}) - (8.2 \pm 0.1);$

$\log_{10}(\gamma(\text{CO on } Fe_2SiO_4)) = (2.3 \pm 0.3) \times 10^{-3}\ T(\text{K}) - (7.7 \pm 0.2);$

$\log_{10}(\gamma(\text{CO on FeOOH/}Fe_2O_3)) = (5.6 \pm 0.8) \times 10^{-3}\ T(\text{K}) - (9.3 \pm 0.4).$

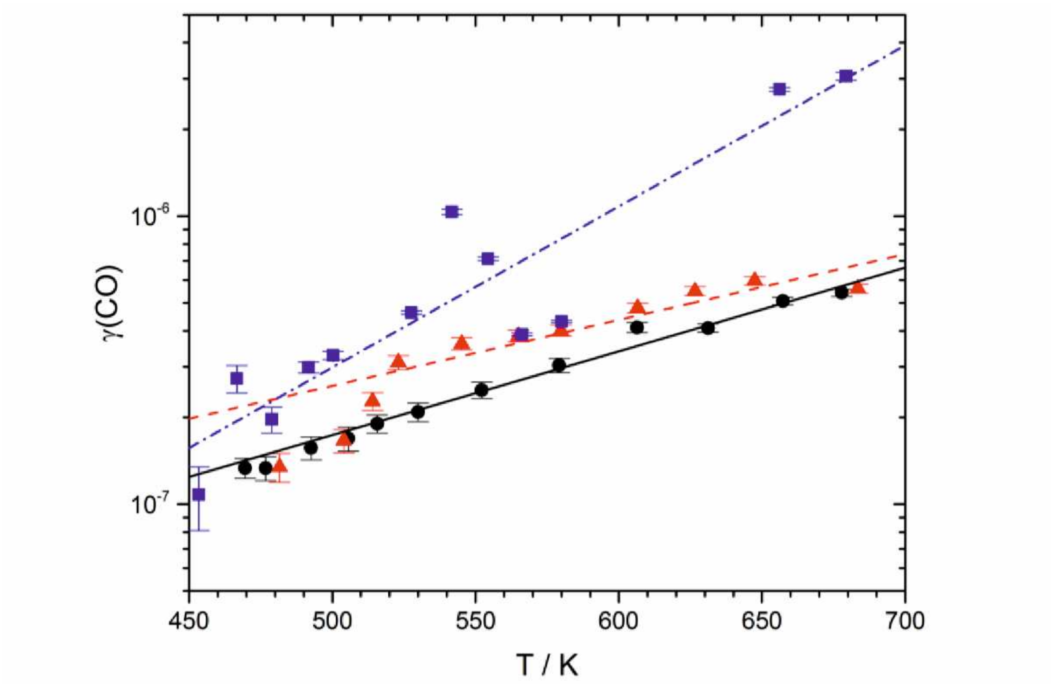

Figure 8. CO uptake coefficient, γ(CO), with respect to temperature for $MgFeSiO_4$ (circles, solid line), Fe_2SiO_4 (triangles, dashed lines) and $FeOOH/Fe_2O_3$ (squares, dash-dot line).

3.6 Electronic structure calculations

We now use quantum theory calculations to examine the heterogeneous reaction mechanism postulated from the experimental results. The hybrid density functional/Hartree-Fock B3LYP method was employed together with the 6-311+G(2d,p) triple zeta basis set, which is a reasonably large, flexible basis set with both polarization and diffuse functions added to the atoms. We have used this level of theory previously for calculations on Fe- and Mg-containing oxides, hydroxides and silicates (Saunders and Plane, 2011; Rapp et al., 2012). The expected uncertainty in the calculated reaction enthalpies is ±20 kJ mol^{-1} at this level of theory. The calculations were performed using the Gaussian 09 suite of programs (Frisch et al., 2009).

The Eley-Rideal mechanism supported by the calculations is illustrated in Figure 9. We first consider the binding of O_2 with exposed surface sites i.e., to either the Fe or Mg end of an $FeMgSiO_4$ unit, followed by reaction with CO. While this is clearly an approximation of the surface, it yields useful insights into the reaction mechanism. For each molecule the geometry was first optimised, and then vibrational frequencies calculated to determine the zero point energy correction. The most stable form of $FeMgSiO_4$ (Figure 9(a)) has quintet spin multiplicity (Saunders and Plane, 2011) because of the presence of the Fe atom. We therefore considered all possible spin multiplicities of the species involved in O_2 uptake and subsequent reaction. The results for the most stable spin states are reported here.

O_2 binds much more strongly to the Fe end of the molecule (binding energy = 146 kJ mol^{-1}), compared with the Mg end (66 kJ mol^{-1}). This is consistent with the observed rate of CO_2 production depending on Fe active sites (Section 3.1). Note that the strong O_2-Fe binding energy ensures that O_2 will adsorb at temperatures as high as 700 K. CO can then attack the adsorbed O_2 (Figure 9(b)) via the transition state (Figure 9(c)) to yield CO_2 and the single adsorbed O in Figure 9(d). Finally, a second CO removes this O via the transition state in Figure 9(e), which then releases the Fe active site for further uptake of O_2. The transition state for attack by the first CO (Figure 9(c)) is 113 kJ mol^{-1} above the reactants $O_2FeMgSiO_4$ + CO. In contrast, the energy barrier for the gas-phase reaction $CO + O_2 \rightarrow CO_2 + O$ is 203 kJ mol^{-1}. This explains why the heterogeneous reaction is significantly faster, and the positive temperature dependence of γ(CO) (Figure 8). The presence of this barrier also supports the conclusion that CO reacting with adsorbed O_2 is the rate determining step, so long as there is significant O_2 to pre-adsorb onto the surface. There is no barrier for the reaction $OFeMgSiO_4$ + CO: the transition state in Figure 9(f) is 3.6 kJ mol^{-1} below the energy of the reactants, because the reaction first involves formation of an $O(CO)FeMgSiO_4$ complex (Figure 9(e)), followed by rearrangement to the CO_2 + $FeMgSiO_4$ products. A final point is that CO binds much less strongly to $FeMgSiO_4$ than O_2: the binding energies are 110 compared with 146 kJ mol^{-1}. This explains why the reaction involves gas-phase CO reacting with adsorbed O_2, in agreement with the finding of Leu et al. (1992) who measured negligible uptake of CO on metal oxides including Fe_2O_3 in the absence of O_2.

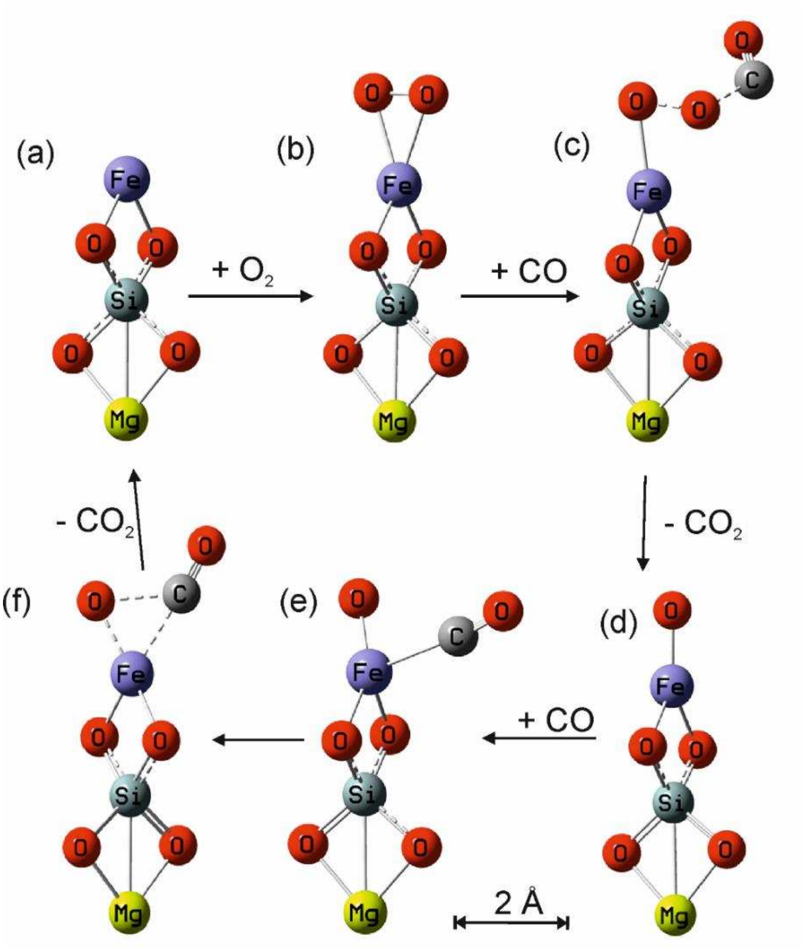

Figure 9. Electronic structure calculations at the B3LYP/6-311+g(2d,p) level of theory, illustrating the oxidation of CO by O_2 on $FeMgSiO_4$: (a) $FeMgSiO_4$, quintet spin multiplicity; (b) O_2 adsorbed on the Fe active site, septet spin multiplicity; (c) transition state for CO_2 formation in the rate-determining step, septet spin multiplicity; (d) singly bound O, quintet spin multiplicity; (e) addition of CO to form a weakly-bound complex, quintet spin multiplicity; (f) transition state for formation of a second CO_2 molecule, quintet spin multiplicity, which regenerates the Fe active site (a).

We now use electronic structure theory to examine two aspects of the possible role of SO_2 in CO oxidation below the clouds on Venus. Firstly, “poisoning” of these dust catalysts by SO_2

binding to the Fe-active sites. In fact, SO_2 also binds much less strongly than O_2, with a binding energy of only 115 kJ mol^{-1}, so that adsorbed SO_2 should be displaced by O_2. The second role of SO_2 is as a gas-phase oxidant of CO in the high temperatures of the Venusian troposphere (Krasnopolsky, 2013). Reaction 4 has been studied in a shock tube between 1770 and 2450 K (Bauer et al., 1971). However, a subsequent theoretical study (Bacskay and Mackie, 2005) found that the reaction barrier on the singlet potential energy surface, calculated at a high level of theory, was 245 kJ mol^{-1}; that is, considerably larger than the activation energy of 202 ± 4 kJ mol^{-1} measured in the shock tube study. In fact, complex kinetics were observed in the flow tube, which Bauer et al. (1971) postulated was due to vibrationally excited SO_2. Bacskay and Mackie (2005) (and earlier theoretical work) demonstrated that trace impurities in the CO_2 could also have been responsible. Since previous theoretical work has focused on temperatures well above 1000 K, we determined the transition state for the reaction in order to calculate an Arrhenius expression for the rate coefficient, k_4, over the 300 – 800 K temperature range applicable to Venus, where the temperature ranges from ~400 to 740 K between 40 km and the surface (Krasnopolsky, 2012). The transition state geometry was first optimized at the B3LYP/6-311+g(2d,p) level for rotational constants and vibrational frequencies. An accurate barrier height of 249 kJ mol^{-1} was then determined at the complete basis set CBS-QB3 level of theory (Frisch et al., 2009), which is in excellent agreement with Bacskay and Mackie (2005). The resulting expression calculated using Transition State Theory is $k_4(300\text{-}800\ \text{K}) = 9.4 \times 10^{-13} \exp(-256\ \text{kJ mol}^{-1}/RT)$ cm^3 molecule^{-1} s^{-1}. It should be noted that k_4 is predicted to be ~4 orders of magnitude smaller at a temperature of 620 K (typical of the lower troposphere around 15 km altitude), than extrapolating from the shock tube result above 1770 K adopted in the model of Krasnopolsky (2013). Of course, the reverse reaction between CO_2 and SO to form SO_2 + CO, which nearly balances in that model, will be reduced by the same factor.

4. Atmospheric Implications

4.1 Modelling the cosmic dust abundance

To study the impact of heterogeneous CO oxidation on meteoric particles in Venus' atmosphere, a 1D model was constructed for the conditions of the dayside. The vertical profiles of temperature, eddy diffusion coefficient (K_{zz}) and pressure were based on Krasnopolsky's 1D model (Krasnopolsky, 2007;2012). The profiles of T and K_{zz} are illustrated in Figure 10.

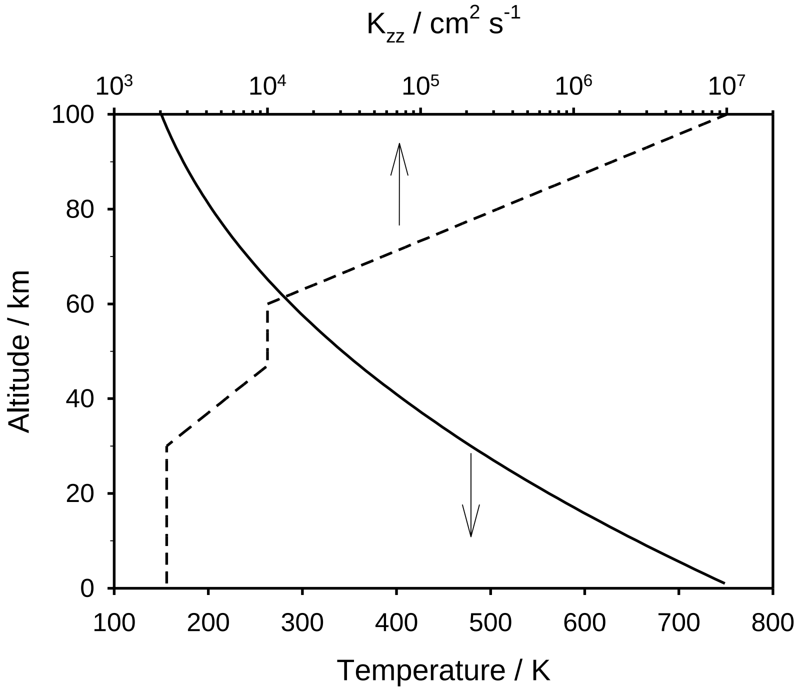

Figure 10. Vertical profiles of temperature and eddy diffusion coefficient (K_{zz}).

The major sources of cosmic dust particles in the inner solar system are the asteroid belt, Jupiter Family comets (JFCs), and Halley Type/Oort Cloud comets. In the Zodiacal Cloud Model (ZCM) developed by Nesvorny et al. (2010), sub-mm particles from these sources are launched and tracked as their orbits evolve under the influence of solar radiation pressure, Poynting-Robertson drag and planetary perturbations. Observations of infra-red emission from the Zodiacal Cloud, measured by the Infrared Astronomical Satellite (IRAS), indicates that the majority (>80%) of the IR emission is produced by particles originating from Jupiter family comets (Nesvorny et al., 2010; Nesvorný et al., 2011).

Here we use a specific version of the ZCM model that was calibrated on several constraints using the methods from Nesvorný et al. (2010; 2011). The size distribution of cosmic dust particles was assumed to be represented by a broken power law with a differential index -2 to -3 below the break diameter D_{break}, and a differential index -4 to -5 above D_{break}. While this is arguably a crude approximation of the real size distribution, it is a good starting point to explore the dependence on D_{break}. The Long Duration Exposure facility (LDEF) results suggested that D_{break}~200 μm for particles accreted by the Earth (e.g. Love and Brownlee (1993)). The Planck telescope, on the other hand, reported weak emission of the Zodiacal Cloud at sub-mm wavelengths (Ade et al., 2014), which has been used to suggest D_{break} <~30 μm (e.g., Fixsen and Dwek (2002)). Note that changes of the assumed size distribution arise because the orbital dynamics/collisional destruction of cosmic particles and their accretion by planets are size dependent.

For the present study, the IRAS observations were used to calibrate the total population of particles in the model, assuming the LDEF size distribution. Particles of different sizes were released from the different sources (e.g., JFCs, asteroids) and their orbits were followed with an N-body code. These integrations accounted for the gravity of all planets, solar pressure, and Poynting-Robertson drag. We used a collisional model where particles were assumed to be destroyed by collisions with other particles in the Zodiacal cloud if they spend a characteristic time, τ, in space. The parameter τ was taken as a function of the particle size and orbit (Nesvorný et al., 2011). The accretion probability of particles on planets was computed with the standard Öpik code (e.g., Greenberg (1982)). The LDEF ZCM with D_{break}~200 μm was found to reproduce the LDEF measurement of the size distribution of accreted particles.

We have recently combined the mass/velocity/radiant distributions of these cosmic dust populations from the ZCM with the Chemical ABlation MODel (CABMOD) (Vondrak et al., 2008), in order to estimate the injection rates of Na and Fe into the Earth's upper atmosphere, as well as the flux of cosmic spherules to the surface (Carrillo-Sánchez et al., 2016). By comparing these parameters to lidar observations of the vertical Na and Fe fluxes, and the measured cosmic spherule accretion rate at South Pole, the absolute contributions from JFCs, the asteroid belt and Halley Type/Oort Cloud comets can be determined for the terrestrial atmosphere and hence in the ZCM (Carrillo-Sánchez et al., 2016). The ZCM can then be applied to Venus. We find that Venus and Earth have similar accretion influx in cosmic particles and that the velocity distribution of accreted particles by both planets is also similar. The total mass of un-ablated cosmic dust into Venus' atmosphere is 32 metric tonnes per earth day (t d^{-1}), with 86% of the mass from JFC particles, 12% from Halley Type/Oort cloud comets, and 2% from the asteroid belt.

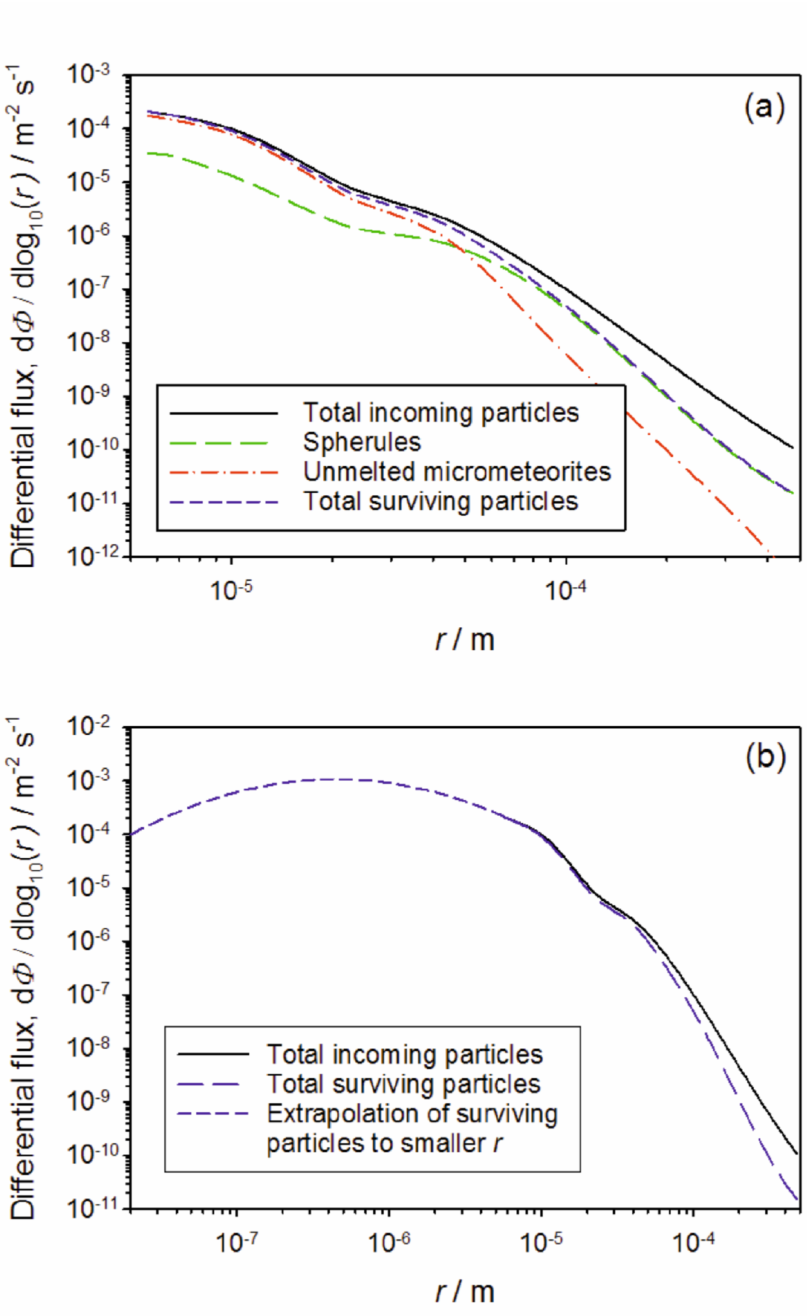

Figure 11. (a) Differential flux of cosmic dust particles into Venus' atmosphere, showing the total flux made up of particles from Jupiter family comets, the asteroid belt, and Halley type comets (black line); particles which form cosmic spherules (green line); particles which do not melt and form micrometeorites (red line); and total surviving particles (blue line). (b) Total incoming particles (black line) and surviving particles (blue line), extrapolated to smaller particle sizes using the parameterisation in eqn. 2.

Figure 11(a) illustrates the differential flux of particles from these sources into Venus' atmosphere. The modelled differential flux can be fit to the following parameterisation of particle radius *r* (in m):

$$\mathrm{d}\phi / \mathrm{dlog}_{10}(r) \ / \ \text{particle m}^{-2}\ \text{s}^{-1} = 10^{\alpha} \qquad (2)$$

where α = -9168.23 - 13841.3x - 8641.28x^2 - 2848.13x^3 - 521.647x^4 - 50.0844x^5 - 1.91675x^6 + 7.203504×10^{-3} x^7, and x = log$_{10}$(*r*). Figure 11(b) shows this parameterisation extrapolated from the particle size range in the ZCM (5 - 500 μm) down to 20 nm. The gradual fall-off in the differential flux of particles < 5μm is expected because solar radiation pressure ejects very small particles from the solar system (Nesvorny et al., 2010). Note that the sharpness of the fall off is uncertain; however, as discussed below, the modelling results of particle number distribution in the atmosphere are not sensitive to the degree of fall off. The dust is assumed to have a density of 2200 kg m^{-3} (Han et al., 2011), and was segregated into 45 size bins increasing geometrically in particle radius from 0.016 to 512 μm.

4.2 Meteoric ablation and the formation meteoric smoke particles

In order to determine the fraction of these dust particles that will ablate, we used CABMOD (Vondrak et al., 2008) to treat meteoric ablation in Venus' atmosphere starting at 500 km. For a given meteoroid mass, velocity and entry angle, CABMOD predicts the ablation rate of individual meteoric elements through sputtering (i.e. through inelastic collisions with atmospheric molecules), and by evaporation of atoms and oxides once the particle melts. The cosmic dust particles were taken to have an olivinic composition, as determined by the analysis of Comet 81P/Wild 2 dust samples (Zolensky et al., 2006; Gainsforth et al., 2015), with an Fe:Mg ratio of ~0.6. According to the olivine phase diagram, the particles should then melt at 1750 K (Vondrak et al., 2008). Figure 12 shows the predicted elemental injection rates integrated over the mass and velocity distributions (10 – 84 km s^{-1}) predicted by the ZCM. The most volatile elements, Na and K, are released about 10 km higher than the main constituents Fe, Si and Mg. The peak ablation rate occurs at an altitude of ~115 km, which is 20 km higher than in the Earth's atmosphere (Vondrak et al., 2008). Out of the 32 t d^{-1} of cosmic dust that enters the atmosphere, 11 t d^{-1} ablates (i.e. vaporizes), 8 t d^{-1} forms cosmic spherules (i.e. the particles melt but do not completely ablate and then solidify), and 13 t d^{-1} remains as unmelted micrometeorites. Figure 11 shows that significant ablation only occurs for particles larger than r = 15 μm, and that spherules become the major form of residual meteoroids for r > 50 μm, although most of these larger particles enter at high enough speeds to ablate completely.

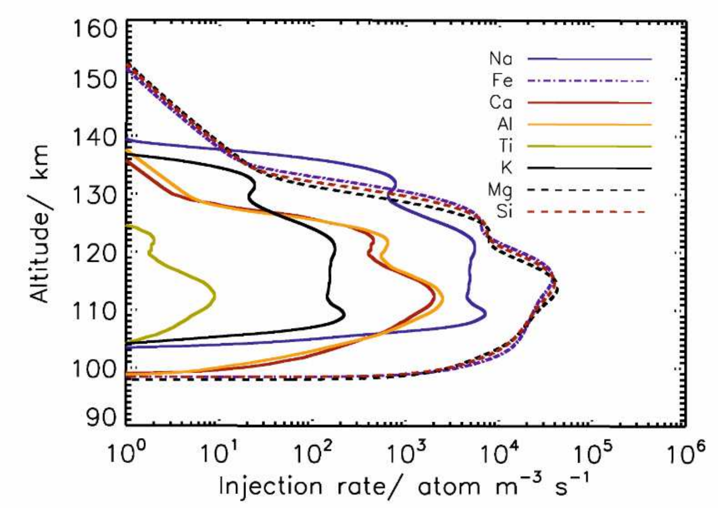

Figure 12. Injection rate profiles for individual elements from meteoric ablation in Venus' atmosphere.

The ablated constituents – principally Fe, Mg and Si atoms – will become oxidized by reactions with O_3, O_2, CO_2, and H_2O to form metal oxide, hydroxide, carbonate and silicate molecules, which then polymerize into meteoric smoke particles (MSPs) (Plane et al., 2015). These sub-nm-sized particles rapidly coagulate into larger particles (Saunders and Plane, 2006). In the present study, particle growth through coagulation was treated using a semi-implicit, volume-conserving model fitted to growth rates measured in the laboratory (Saunders and Plane, 2006) . Growth occurs through a number of discrete size bins where the first bin size (r_1 = 0.20 nm) corresponds to the radius of a single monomer. Growth is then assumed to be dominated by Brownian diffusion-coagulation where collisions between pairs of particles result in coalescence, maintaining spherical morphology and compact structure (particle density = 2200 kg m^{-3}). The collision rate coefficients (or kernels) for Brownian coagulation of these small particles are calculated using the expression for the free molecular regime (Knudsen number, $K_n >> 1$), interpolated into the transition regime for larger particles (Fuchs, 1964).

The flux of dust particles of different sizes being transported vertically by eddy diffusion and sedimentation is given by:

$$\phi_i = -K_{zz}\left\{\frac{\partial N_i}{\partial z} + \left(\frac{1}{T}\frac{\partial T}{\partial z} + \frac{1}{H}\right)N_i\right\} + w_i N_i \tag{3}$$

where ϕ_i is the vertical flux of particles in dust size bin *i*, K_{zz} is the eddy diffusion coefficient, *z* is the altitude coordinate, N_i is the dust number density, *H* is the atmospheric scale height, and w_i is the sedimentation velocity. w_i can be determined from a form of Stokes' law which describes a spherical particle falling through a stationary fluid (Jacobson, 2005):

$$w_i = \frac{2(\rho_{dust}-\rho_{air})}{9\mu} g\, r_i^2 C_{scf} \tag{4}$$

where ρ_{dust} and ρ_{air} are the dust and air density; μ is the dynamic viscosity of CO_2 at temperature T; g is the gravitational constant (8.87 m s^{-2} for Venus); r_i is the particle radius and C_{scf} is the Cunningham slip correction factor which takes into account the non-continuum effects of drag on small particles. C_{scf} is estimated from equation 5, where λ is the mean free path of the CO_2 molecules, and A_1, A_2 and A_3 are dimensionless coefficients (Kasten, 1968).

$$C_{scf} = 1 + \frac{\lambda}{r_i}\left(A_1 + A_2 exp\left(\frac{-A_3 r_i}{\lambda}\right)\right) \qquad (5)$$

Equation 3 was solved using a time-implicit integration scheme (Shimazaki, 1985). Figure 13 shows the resulting size distributions of particle number density (N) and volumetric surface area (A_s), as a function of height between the surface and 80 km. Most of the available surface area for heterogeneous chemistry is between 40 and 70 km, and is provided by small particles ($r < 0.2$ μm). The highest values of A_s are therefore located in the same atmospheric region as the cloud layer on Venus (Knollenberg and Hunten, 1980). The dust number density and surface area decrease in the troposphere because of coagulation, which is exacerbated by the increasingly slow rate of sedimentation as the atmospheric density increases.

Knollenberg and Hunten (1980) used a particle size spectrometer on the Pioneer Venus sounder to determine a particle number density of 20 particles cm^{-3} with a mean radius of 0.1 μm in the lower haze layer around 35 km, although the instrument could actually only measure particles larger than $r = 0.3$ μm. The present model predicts a total of 117 smoke particles cm^{-3} at 35 km. However, these coagulated smoke particles have a mean radius of only 0.04 μm, and the concentration of smoke particles with $r > 0.1$ μm is 1.8 cm^{-3} (1.6×10^{-4} cm^{-3} for $r > 0.3$ μm), which would have been undetectable with the particle spectrometer.

To test the sensitivity of the aerosol model to the degree of fall-off in the differential flux of small meteoroids, the extrapolated flux in Figure 11(b) was reduced by a factor of 100 for all incoming particles < 5 μm. In fact, this makes essentially no difference to the particle number and surface area densities in Figure 13. The reason is that it is only particles > 5 μm that ablate, and it is this ablated vapour that then produces the MSPs which contribute most of the available surface area for chemistry. This is evident in Figure 13: most of the surface area is carried by particles smaller than 0.2 μm, which first appear via coagulation around 70 km.

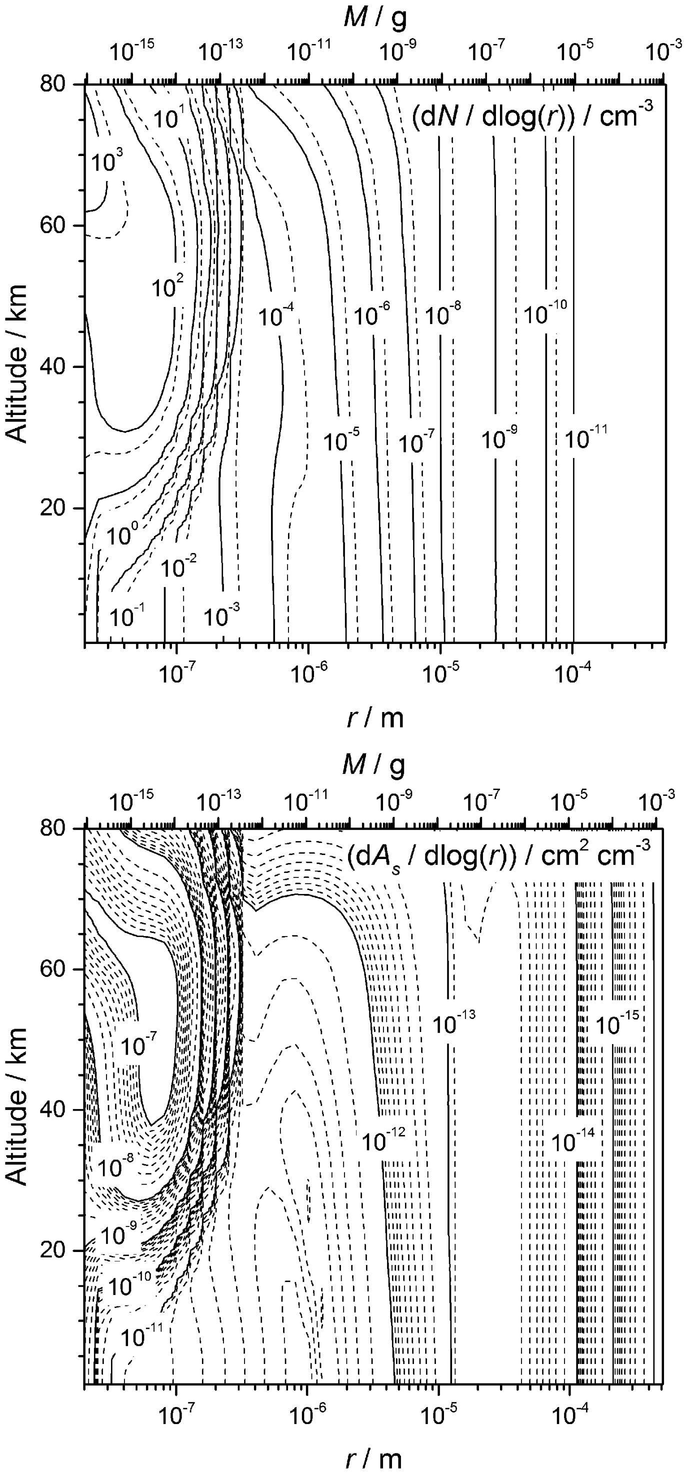

Figure 13. A plot of the size distribution of dust particle number density, N, (top panel) and volumetric surface area, A_s, (bottom panel) as a function of altitude.

4.3 Oxidation of CO

The CO mixing ratio as a function of height *z* in the model was initially set to a polynomial functional fit to various literature sources (Hedin et al., 1983; Krasnopolsky, 2012;2013): $\log_{10}(\chi(\mathrm{CO})/\mathrm{ppm}) = 0.96 + 0.026z - 5.0\times10^{-4} z^2 + 3.7\times10^{-6} z^3$, where *z* is in km. The O_2 mixing ratio in the model is fixed to 0.7 ppm above 67 km, so that the column abundance above the cloud tops (67 km) is 6 x 10^{17} cm^{-2}, which is just over 50% of the upper limit determined by Trauger and Lunine (1983). The reason for fixing the O_2 above the cloud tops is that the heterogeneous removal on meteoric smoke is only significant at the higher temperatures in the troposphere below 40 km. Between 67 km and the surface the O_2 density was initially set to the value at 67 km (1.0×10^{12} cm^{-3}). The SO_2 mixing ratio is set to 130 ppm up to the cloud base at 48 km (Bezard et al., 1993).

For the CO uptake kinetics, the temperature-dependent expression for γ(CO on $MgFeSiO_4$) was used (Section 3.5). This means that CO oxidation only becomes significant at temperatures above about 400 K. We assume here that any chemical processing of the small meteoric dust particles which sediment slowly through the H_2SO_4 clouds, thereby reducing their catalytic activity by forming Fe sulphates, is reversed at the higher temperatures below the clouds where the particles will convert into Fe_2O_3 which is catalytically active (section 3.1). $\gamma(O_2)$ was varied from 1 x 10^{-5} (just below the lower limit from the laboratory investigation in Section 3.3 – see Figure 5) to 1×10^{-3}, with no temperature dependence. As discussed in Section 3.4, the rate determining step in the experimental measurements of CO oxidation was the reaction of CO with an adsorbed O_2 molecule. Note, however, that the laboratory measurement of γ(CO) was under conditions where the rate was independent of $[O_2]$. In an O_2-poor region of the atmosphere the rate of O_2 uptake could become rate-determining and therefore control the CO oxidation rate, especially since CO has been found to bind poorly to Fe_2O_3 in the absence of O_2 (Leu et al., 1992). In the model, the rate of CO oxidation was therefore set to whichever was slower: either twice the rate of O_2 uptake (since each O_2 oxidizes 2 CO), or the uptake rate of CO. The vertical continuity equations for CO, O_2 and CO_2 were then solved between 0 and 90 km, and the concentrations of these species fixed above 90 km (where heterogeneous uptake is unimportant because of a relatively small A_s and low temperatures).

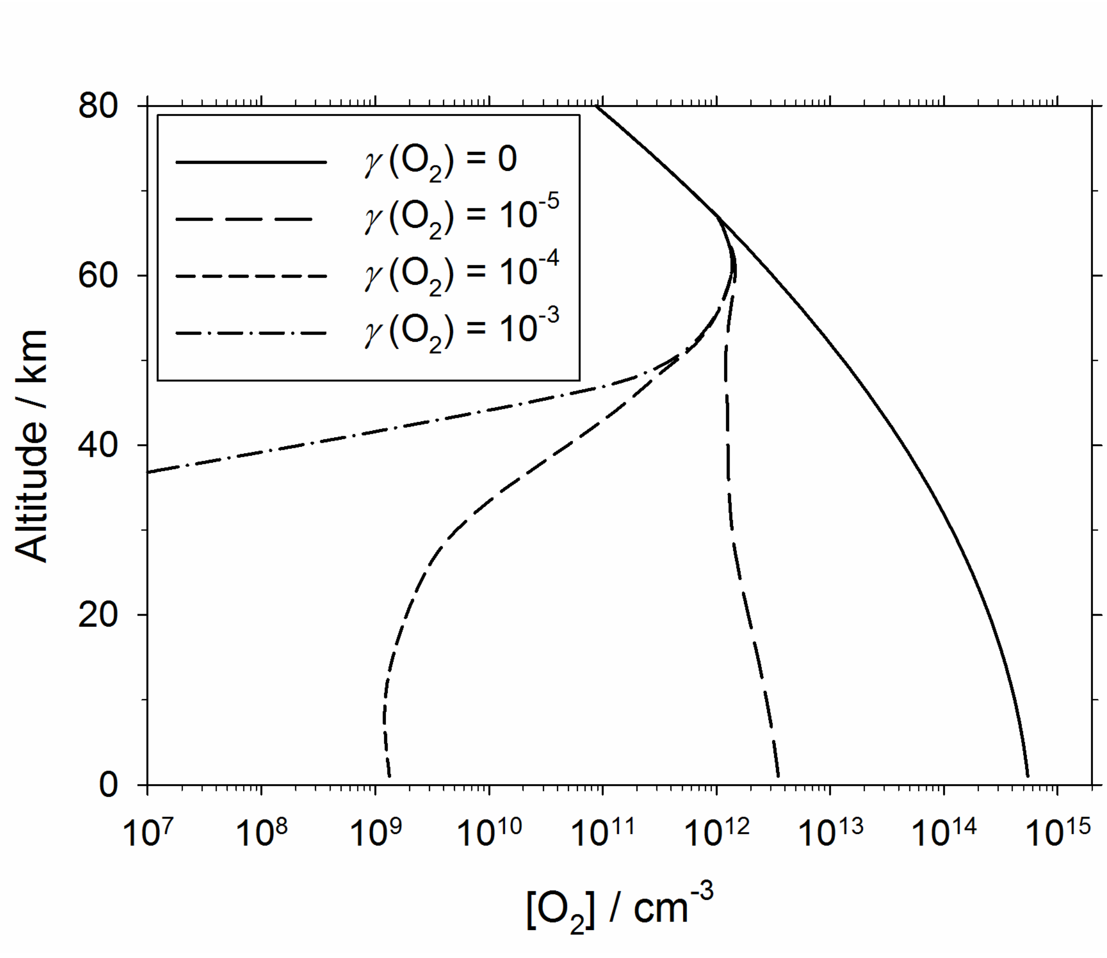

Figure 14. Modelled profiles of the O_2 density, for different values of $\gamma(O_2)$. Note that the O_2 concentration is fixed above 67 km.

Figure 14 shows the modelled O_2 density after the model has reached steady-state, for a range of $\gamma(O_2)$. As discussed in Section 3, the lower limit for $\gamma(O_2)$ deduced from the flow tube experiments is 2×10^{-5}, which would reduce O_2 by more than 1 order of magnitude below 45 km. If γ is only a factor of 5 larger, the reduction would be at least 3 orders of magnitude larger below 30 km. If $\gamma(O_2)$ is $> 10^{-4}$ then there is sufficient meteoric dust to remove O_2 almost completely below 40 km, because the rate of uptake is fast enough to compete with the downward transport of O_2 from higher altitudes by eddy diffusion. Note that there is a decrease of O_2 between 40 and 67 km, which occurs because of more rapid downward transport of O_2 from the region where it is produced photochemically to the region below 40 km where O_2 is depleted by heterogeneous CO oxidation. However, the decrease is insufficient to account for the over-prediction of O_2 that has been noted in models with full chemistry (Krasnopolsky, 2012), rather than prescribed O_2 above 67 km as in the present model.

Figure 15 shows the corresponding CO oxidation rates for the same range of $\gamma(O_2)$. The rates all decrease below ~40 km because of the smaller available dust surface area (Figure 13). Note that the CO oxidation rate is higher at lower $\gamma(O_2)$, because the O_2 below 40 km is less depleted (Figure 14). However, Figure 15 shows that even at the highest value of $\gamma(O_2)$, the heterogeneous oxidation rate is still faster above 20 km than the gas-phase SO_2 oxidation rate calculated using the theoretical rate coefficient k_4 derived in Section 3.5. The rate coefficient for the gas-phase reaction between CO and O_2 has been measured reliably at temperatures above 1500 K, yielding the Arrhenius expression $k(CO + O_2) = 4 \times 10^{-12} \exp(-200 \text{ kJ mol}^{-1}/ RT)$ $\text{cm}^3 \text{ molecule}^{-1} \text{ s}^{-1}$ (Tsang and Hampson, 1986). Extrapolating down to temperatures below 750 K indicates that this gas-phase CO oxidation reaction is a factor of 40 slower than the heterogeneous oxidation (for $\gamma(O_2) = 10^{-4}$) 5 km above the planet's surface, and insignificant at higher altitudes.

Krasnopolsky (2012) has modelled the gas-phase chemistry of CO between 47 and 112 km. Compared with Figure 2 in his paper, the heterogeneous oxidation of CO below 60 km is significantly faster than the reactions with Cl (reaction 1) and OH (reaction2). However, at 70 km these reactions are 2500 and 20 times faster than the heterogeneous reaction, respectively. Since most of the CO in Venus' atmosphere is produced by photolysis of CO_2 above 70 km (Krasnopolsky, 2012), this means that heterogeneous oxidation of CO at lower altitudes is relatively unimportant.

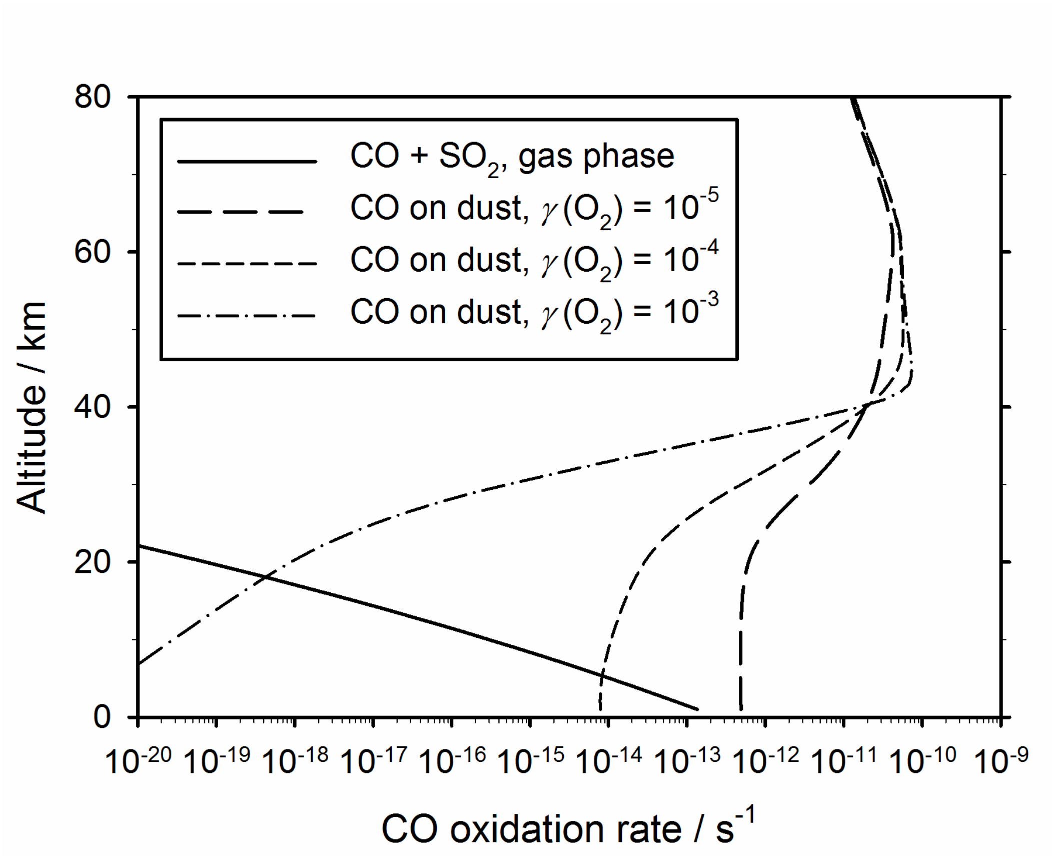

Figure 15. The rate of CO oxidation through heterogeneous reaction on dust, modelled for three values of $\gamma(O_2)$, compared with the gas-phase oxidation by SO_2.

5. Conclusions

The kinetics of CO oxidation on a selection of dust particles which are possible analogues of meteoric material in Venus' atmosphere (Mg_2SiO_4, $MgFeSiO_4$, Fe_2SiO_4, $FeOOH/Fe_2O_3$, $Fe_2(SO_4)_3$ and $FeSO_4$) were studied over an appropriate temperature range (300 - 680 K). The reaction appears to follow the Eley-Rideal surface mechanism with O_2 chemisorbed onto Fe active sites (no measurable CO_2 was formed on Mg_2SiO_4). The CO oxidation reaction step was found to be rate determining on all of the Fe-bearing dust except for $Fe_2(SO_4)_3$ and $FeSO_4$, where the two Fe sulfates had to first decompose into Fe oxides at around 540 K before CO oxidation could occur.

A 1-D atmospheric model of Venus was then constructed to explore the role of heterogeneous oxidation. The cosmic dust input to Venus, mostly originating from Jupiter Family Comets, is found to be ~32 tonnes per Earth day. A chemical ablation model was then used to show that ~34% of this incoming mass ablates, forming meteoric smoke particles. Above Venus' clouds, the temperature is too low for catalysis by olivinic smoke surfaces to be significant; however, below 40 km, together with unablated dust particles, smoke provides a significant surface for the heterogeneous oxidation of CO to CO_2, and the corresponding removal of O_2. Although this process has a minor effect on CO because it is in large excess over O_2 (by a factor > 50), substantial removal of O_2 below 40 km is predicted.

Theoretical calculations indicate that the oxidation of CO by SO_2 in Venus' lower troposphere is about 4 orders of magnitude slower than previous work which extrapolated from a high-temperature shock tube study, and so this reaction is not competitive with the heterogeneous oxidation of CO measured in this study.

In conclusion, this study appears to be the first attempt to quantify the surface area of meteoric smoke particles and unablated micro-meteorites available in Venus' atmosphere for heterogeneous chemistry. Here we have focused on a high-temperature process (CO oxidation), which should occur in the troposphere below 40 km. However, other surface-catalyzed processes involving acidic gases and photochemical radicals, which occur on smoke analogues at temperatures below 300 K (Frankland et al., 2015; James et al., 2017) , may be important even above the clouds, where a significant surface area of meteoric smoke is predicted to be available (Figure 13). It is also worth noting that it may be possible to observe the smoke particles in this region by optical extinction from satellite-borne spectrometers, as in the terrestrial mesosphere (Hervig et al., 2009). Finally, the present study demonstrates the importance of laboratory measurements for quantifying the kinetics of heterogeneous processes in models.

6. Acknowledgements

This work was supported by funding from the Leverhulme Trust (grant F/00 122/BB – PETALS) and the European Research Council (project number 291332 – CODITA). The authors acknowledge Dr Bruce Turnbull (University of Leeds) for advice regarding the purification of the sol-gel particles and Drs Martin Schnaiter and Robert Wagner (Karlsruhe Institute of Technology) for their help in characterising the MSP analogues. The experimental and modelling data used in this study is available on request from JMCP.

References

Ade, P. A. R., et al., 2014. Planck 2013 results. XIV. Zodiacal emission. Astron. Astrophys. 571**,** art. no.: A14.

Anderson, J. L., Peterson, R. C., Swainson, I. P., 2007. The atomic structure and hydrogen bonding of deuterated melanterite, $FeSO_4.7D_2O$. Canadian Mineralogist. 45**,** 457-469.

Bacskay, G. B., Mackie, J. C., 2005. Oxidation of CO by SO_2: A Theoretical Study. J. Phys. Chem. A. 109**,** 2019-2025.

Bauer, S. H., Jeffers, P., Lifshitz, A., Yadava, B. P., 1971. Reaction between CO and SO_2 at Elevated Temperatures: A Shock-Tube Investigation. Symp. Int. Combust. Proc. 13.

Bezard, B., et al., 1993. The abundance of sulfur dioxide below the clouds of Venus. Geophys. Res. Lett. 20**,** 1587–1590.

Bezard, B., de Bergh, C., 2007. Composition of the atmosphere of Venus below the clouds. J. Geophys. Res. 112**,** art. no. E04S07.

Bulgakov, N. N., Sadykov, V. A., 1996. Surface energies of hematite faces and heats of oxygen adsorption: Calculations by modified semiempirical interacting bonds method. React. Kinet. Catalys. Lett. 58**,** 397-402.

Carrillo-Sánchez, J. D., Nesvorný, D., Pokorný, P., Janches, D., Plane, J. M. C., 2016. Sources of Cosmic Dust in the Earth's Atmosphere. Geophys. Res. Lett. submitted.

Cornell, R. M., Schwertmann, U., 2003. The Iron Oxides: Structure, Properties, Reactions, Occurrences and Uses. Wiley-VCH, Weinheim.

Cudennec, Y., Lecerf, A., 2005. Topotactic transformations of goethite and lepidocrocite into hematite and maghemite. Solid State Sci. 7**,** 520-529.

Fegley, B., Zolotov, M. Y., Lodders, K., 1997. The oxidation state of the lower atmosphere and surface of Venus. Icarus. 125**,** 416-439.

Fixsen, D. J., Dwek, E., 2002. The Zodiacal Emission Spectrum as Determined by *COBE* and Its Implications. Astrophys. J. 578**,** 1009-1014.

Frankland, V. L., Alexander, J. D., Feng, W., Plane, J., 2015. The uptake of HNO_3 on meteroic smoke analogues. Journal of atmospheric and solar-terrestrial physics. 127**,** 150-160.

Frisch, M. J., et al., 2009. Gaussian 09, Revision A. 01, Gaussian. Inc., Wallingford, CT.

Fuchs, N. A., 1964. Mechanics of Aerosols. Pergamon, New York.

Gainsforth, Z., et al., 2015. Constraints on the formation environment of two chondrule-like igneous particles from comet 81P/Wild 2. Meteor. Planet. Sci. 50**,** 976-1004.

Greenberg, R., 1982. Orbital interactions - A new geometrical formalism. Astron. J. 87, 184-195.

Grenfell, J. L., Stock, J. W., Patzer, A. B. C., 2013. CO-oxidation on surface hematite in hot atmospheres of rocky planets. Planet. Space Sci. 84, 14-19.

Grenfell, J. L., Stock, J. W., Patzer, A. B. C., Gebauer, S., Rauer, H., 2010. Oxidation of CO on surface hematite in high CO_2 atmospheres. Planet. Space Sci. 58, 1252-1257.

Han, D., Poppe, A. R., Piquette, M., Grun, E., Horanyi, M., 2011. Constraints on dust production in the Edgeworth-Kuiper Belt from Pioneer 10 and New Horizons measurements. Geophys. Res. Lett. 38.

Hazen, R. M., 1977. Effects of temperature and pressure on the crystal structure of ferromagnesian olivine. Am. Mineral. 62, 286-295.

Hedin, A. E., Niemann, H. B., Kasprzak, W. T., Seiff, A., 1983. Global empirical model of the Venus thermosphere. J. Geophys. Res. 88, 73-83.

Hervig, M. E., et al., 2009. First Satellite Observations of Meteoric Smoke in the Middle Atmosphere. Geophys. Res. Lett. 36, L18805.

Jacobson, M. Z., 2005. Fundamentals of Atmospheric Modeling, 2nd edn. Cambridge Univ. Press, New York.

James, A. D., Frankland, V. L. F., Rodríguez, J. M. T., Azcárate, J. A., Martín, J. C. G., Plane, J. M. C., 2016. Synthesis and Characterisation of Analogues for Interplanetary Dust and Meteoric Smoke Particles. J. Atmos. Solar-Terr. Phys. under review.

James, A. D., et al., 2017. The uptake of HO2 on meteoric smoke analogues. J. Geophys. Res. 122, 554–565.

Kašpar, J., Fornasiero, P., Hickey, N., 2003. Automotive catalytic converters: current status and some perspectives. Catalysis Today. 77, 419-449.

Kasten, F., 1968. Falling speed of aerosol particles. J. App. Meteor. 7, 944-947.

Khedr, M. H., Halim, K. S. A., Nasr, M. I., El-Mansy, A. M., 2006. Effect of temperature on the catalytic oxidation of CO over nano-sized iron oxide. Mater. Sci. Eng. A. 430, 40-45.

Knollenberg, R. G., Hunten, D. M., 1980. The Microphysics of the Clouds of Venus: Results of the Pioneer Venus Particle Size Spectrometer Experiment. J. Geophys. Res. 85, 8039-8058.

Kolasinski, K., 2002. Surface Science: Foundations of Catalysis and Nanoscience. Wiley.

Krasnopolsky, V. A., 2007. Chemical kinetic model for the lower atmosphere of Venus. Icarus. 191, 25-37.

Krasnopolsky, V. A., 2012. A photochemical model for the Venus atmosphere at 47-112 km. Icarus. 218, 230-246.

Krasnopolsky, V. A., 2013. S_3 and S_4 abundances and improved chemical kinetic model for the lower atmosphere of Venus. Icarus. 225, 570–580.

Leu, M. T., Blamont, J. E., Anbar, A. D., Keyser, L. F., Sander, S. P., 1992. Adsorption of CO on oxide and water ice surfaces: Implications for the Martian atmosphere. J. Geophys. Res.: Planets. 97, 2621-2627.

Li, P., Miser, D. E., Rabiei, S., Yadav, R. T., Hajaligol, M. R., 2003. The removal of carbon monoxide by iron oxide nanoparticles. Appl. Catal. B. 43, 151-162.

Love, S. G., Brownlee, D. E., 1993. A Direct Measurement of the Terrestrial Mass Accretion Rate of Cosmic Dust. Science. 262, 550–553.

Mills, F. P., Allen, M., 2007. A review of selected issues concerning the chemistry in Venus' middle atmosphere. Planet. Space Sci. 55, 1729–1740.

Nesvorný, D., Janches, D., Vokrouhlický, D., Pokorny, P., Bottke, W. F., Jenniskens, P., 2011. Dynamical Model for the Zodiacal Cloud and Sporadic Meteors. Astrophys. J. 743, 129.

Nesvorny, D., Jenniskens, P., Levison, H. F., Bottke, W. F., Vokrouhlicky, D., Gounelle, M., 2010. Cometary Origin of the Zodiacal Cloud and Carbonaceous Micrometeorites. Implications for Hot Debris Disks. Astrophys. J. 713, 816-836.

Oyama, V. I., Carle, G. C., Woeller, F., Pollack, J. B., Reynolds, R. T., Craig, R. A., 1980. Pioneer Venus gas chromatography of the lower atmosphere of Venus. J. Geophys. Res. 85, 7891-7902.

Pernice, H., et al., 2004. Laboratory evidence for a key intermediate in the Venus atmosphere: Peroxychloroformyl radical. Proc. Nat. Acad. Sci. 101, 14007–14010.

Plane, J. M. C., Feng, W., Dawkins, E. C. M., 2015. The Mesosphere and Metals: Chemistry and Changes. Chem. Rev. 115, 4497-4541.

Randall, H., Doepper, R., Renken, A., 1997. Modelling CO oxidation on silica-supported iron oxide under transient conditions. Ind. Eng. Chem. Res. 36, 2996-3001.

Rapp, M., et al., 2012. In situ observations of meteor smoke particles (MSP) during the Geminids 2010: constraints on MSP size, work function and composition. Ann. Geophys. 30, 1661-1673.

Saunders, R. W., Dhomse, S., Tian, W., Chipperfield, M., Plane, J., 2012. Interactions of meteoric smoke particles with sulphuric acid in the Earth's stratosphere. Atmos. Chem. Phys. 12, 4387-4398.

Saunders, R. W., Plane, J. M. C., 2006. A laboratory study of meteor smoke analogues: Composition, optical properties and growth kinetics. J. Atmos. Solar-Terr. Phys. 68, 2182-2202.

Saunders, R. W., Plane, J. M. C., 2011. A photo-chemical method for the production of olivine nanoparticles as cosmic dust analogues. Icarus. 212, 373-382.

Shimazaki, T., 1985. Minor Constituents in the Middle Atmosphere. D. Reidel Publishing Company, Dordrecht.

Taylor, F. W., 2010. Planetary Atmospheres. Oxford University Press, Oxford.

Traub, W. A., Carleton, N. P., 1974 Observations of O_2, H_2O, and HD in Planetary Atmospheres. In: A. Woszczyk, C. Iwaniszewska, (Eds.), Exploration of the Planetary System. Reidel, Dordrecht, The Netherlands, pp. 223-228.

Trauger, J. T., Lunine, J. I., 1983. Spectroscopy of molecular oxygen in the atmospheres of Venus and Mars. Icarus. 55, 272–281.

Tsang, W., Hampson, R. F., 1986. Chemical kinetic database for combustion chemistry.1. Methane and related compounds. J. Phys. Chem. Ref. Data. 15, 1087-1279.

von Zahn, U., Kumar, S., Niemann, H., Prinn, R., 1983 Composition of the Venus atmosphere. In: D. M. Hunten, L. Colin, T. M. Donahue, V. I. Moroz, (Eds.), Venus. University of Arizona Press, Tucson, pp. 299-430.

Vondrak, T., Plane, J. M. C., Broadley, S., Janches, D., 2008. A chemical model of meteoric ablation. Atmos. Chem. Phys. 8, 7015-7031.

Wagloehner, S., Reichert, D., Leon-Sorzano, D., Balle, P., Geiger, B., Kureti, S., 2008. Kinetic modeling of the oxidation of CO on Fe_2O_3 catalyst in excess of O_2. J. Catalysis. 260, 305-314.

Wang, D., 2006 Characterisation of catalysts by transmission electron microscopy. In: T. E. Weirich, J. L. Labar, X. Zou, (Eds.), Electron Crystallography: Novel Approaches for Structure Determination of Nanosized Materials. Springer, Dordrecht, pp. 473-487.

Wu, P., Du, P., Zhang, H., Cai, C. X., 2015. Graphyne-supported single Fe atom catalysts for CO oxidation. Phys. Chem. Chem. Phys. 17, 1441-1449.

Zolensky, M. E., et al., 2006. Report - Mineralogy and petrology of comet 81P/Wild 2 nucleus samples. Science. 314, 1735-1739.